MOIRCS Deep Survey. IX.
Deep Near-Infrared Imaging Data and Source Catalog

Masaru Kajisawa[1], Takashi Ichikawa[2], Ichi Tanaka[3], Toru Yamada[2], Masayuki Akiyama[2], Ryuji Suzuki[3],
Chihiro Tokoku[2], Yuka Katsuno Uchimoto[4], Masahiro Konishi[4], Tomohiro Yoshikawa[5], Tetsuo Nishimura[3],
Koji Omata[3], Masami Ouchi[6], Ikuru Iwata[7], Takashi Hamana[8], Masato Onodera[9,10]
kajisawa@cosmos.ehime-u.ac.jp
[1] *Research Center for Space and Cosmic Evolution, Ehime University, Bunkyo-cho 2-5, Matsuyama 790-8577, Japan*
[2] *Astronomical Institute, Tohoku University, Aramaki, Aoba, Sendai 980–8578, Japan*
[3] *Subaru Telescope, National Astronomical Observatory of Japan, 650 North Aohoku Place, Hilo, HI 96720, USA*
[4] *Institute of Astronomy, University of Tokyo, Mitaka, Tokyo 181–0015, Japan*
[5] *Koyama Astronomical Observatory, Kyoto Sangyo University, Motoyama, Kamigamo, Kita-ku, Kyoto 603–8555, Japan*
[6] *Observatories of the Carnegie Institution of Washington, 813 Santa Barbara Street, Pasadena, CA 91101, USA*
[7] *Okayama Astrophysical Observatory, National Astronomical Observatory of Japan, Kamogata, Asakuchi, Okayama,
719–0232, Japan*
[8] *National Astronomical Observatory of Japan, Mitaka, Tokyo 181–8588, Japan*
[9] *Service d'Astrophysique, CEA Saclay, Orme des Merisiers, 91191 Gif-sur-Yvette Cedex, France*
[10] *Institute for Astronomy, ETH Zurich, Wolfgang-Pauli-strasse 27, 8093 Zurich, Switzerland*

Abstract

We present deep J-, H-, and K_s-band imaging data of the MOIRCS Deep Survey (MODS), which was carried out with Multi-Object Infrared Camera and Spectrograph (MOIRCS) mounted on the Subaru telescope in the GOODS-North region. The data reach 5σ total limiting magnitudes for point sources of $J = 23.9$, $H = 22.8$, and $K_s = 22.8$ (Vega magnitude) over 103 arcmin^2 (wide field). In 28 arcmin^2 of the survey area, which is ultra deep field of the MODS (deep field), the data reach the 5σ depths of $J = 24.8$, $H = 23.4$, and $K_s = 23.8$. The spatial resolutions of the combined images are FWHM ~ 0.6 arcsec and ~ 0.5 arcsec for the wide and deep fields in all bands, respectively. Combining the MODS data with the multi-wavelength public data taken with the HST, Spitzer, and other ground-based telescopes in the GOODS field, we construct a multi-wavelength photometric catalog of K_s-selected sources. Using the catalog, we present K_s-band number counts and near-infrared color distribution of the detected objects, and demonstrate some selection techniques with the NIR colors for high redshift galaxies. These data and catalog are publicly available via internet.

Key words: catalogs — galaxies:high-redshift — galaxies:photometry — infrared:galaxies — surveys

1. Introduction

In recent years, several deep multi-wavelength surveys have been carried out to reveal galaxy formation and evolution in the high-redshift universe. Representative examples of such surveys are the Great Observatories Origins Deep Survey (GOODS, Giavalisco et al. 2004), the Subaru XMM-Newton Deep Survey (SXDS, K. Sekiguchi et al., in preparation), the Cosmic Evolution Survey (COSMOS, Scoville et al. 2007), and the All-wavelength Extended Groth strip International Survey (AEGIS, Davis et al. 2007). Deep multi-wavelength observations from radio to X-ray allow us to comprehensively investigate the properties of stars, gas, dust, and AGN of high-redshift galaxies. In such multi-wavelength surveys for high-redshift galaxies, near-infrared (NIR) imaging is essential for the following reasons. First, the observed NIR luminosity of galaxies reflects their stellar mass, which is one of the most basic physical properties of galaxies, relatively well for galaxies at $z \lesssim 3$. NIR data also covers the Balmer/4000Å

break of galaxies at $1 \lesssim z \lesssim 4$, which is important to study the stellar population of these galaxies and to determine their photometric redshifts. Compared to optical light, observed NIR light is less sensitive to the effect of dust extinction, and the spatial resolution of NIR data is comparatively good even in ground-based observations. These are helpful for the identification of sources detected in other wavelengths such as X-ray, mid-IR, sub-mm and radio.

The recent availability of wide-field NIR instruments with large-format detectors mounted on 4-8m telescopes has allowed us to carry out wider and deeper NIR surveys. With such new instruments, we still need a relatively long integration time in order to construct a representative sample of high-redshift galaxies. For example, a normal L* galaxy seen in the local universe would have $K_{\rm Vega} \sim 23$ if placed at $z \sim 3$ (e.g., Franx et al. 2003). Deeper data would be desirable for the investigation of low-mass (sub-L*) galaxies at such high redshift. The search for star-forming galaxies at $z \gtrsim 7$ also
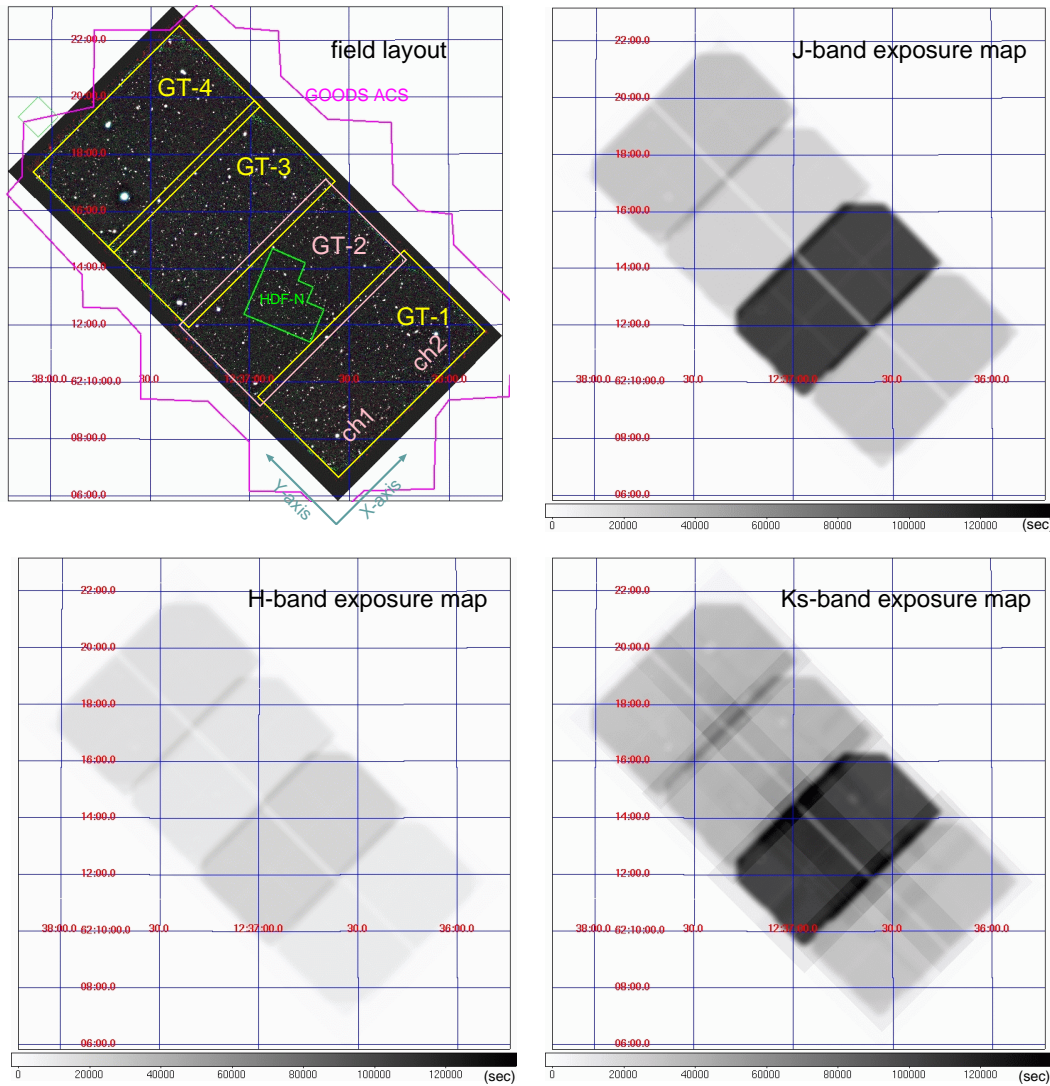
Fig. 1. Survey field layout and exposure maps for J, H, and K_s bands. In the top-left panel, the GOODS-N HST/ACS region and the original HDF-N region are shown in magenta and green lines. Arrows represent the direction of X- and Y-axes of the mosaiced MOIRCS images. Grayscales in the top-right, bottom-left and bottom-right panels show the integration time of the MOIRCS J, H, and K_s-band imaging, respectively.

requires extremely deep NIR data. Existing NIR surveys with such depth are limited to several small field surveys. They include those with the Hubble Space Telescope (HST)/NICMOS such as Hubble Deep Field North (HDF-N; Dickinson et al. 2003; Thompson et al. 1999), HDF-South NICMOS field (Williams et al. 2000), and Hubble Ultra Deep Field (UDF, Thompson et al. 2005). The new HST instrument, WFC3 IR-channel is providing deeper data than those with NICMOS (e.g., Windhorst et al. 2010), but the deep NIR observations with the HST instruments are practically limited to $\lambda < 1.8\mu$m. Although there are also ultra-deep NIR surveys with ground-based 8m class telescopes such as Subaru Deep Field (Maihara et al. 2001) and Faint Infrared Extragalactic Survey HDF-S field (FIRES; Labbé et al. 2003), these surveys have small fields of several arcmin^2.

We have carried out a ultra-deep NIR imaging survey, namely, MOIRCS Deep Survey (MODS) with Multi-Object Infrared Camera and Spectrograph (MOIRCS) mounted on the Subaru telescope in the GOODS-North region. Total integration time of $\sim$ 124 hours were spent in the JHK_s-band imaging observations with MOIRCS, and the data reach $K_s \sim 23$ (5σ, Vega) over $\sim$ 103 arcmin^2, and $K_s \sim 24$ over $\sim$ 28 arcmin^2. In this region, the GOODS and the Chandra Deep Field North (CDF-N) surveys provided deep multi-wavelength imaging data such as optical HST/ACS images (Giavalisco et al. 2004), mid-IR images obtained with Spitzer/IRAC and MIPS (M. Dickinson et al., in preparation), and Chandra X-ray images (Alexander et al. 2003). Extremely deep radio observations with VLA, deep sub-mm/mm surveys with SCUBA, AzTEC and MAMBO, and extensive optical spectroscopic surveys with the Keck telescopes have also been carried out (e.g., Morrison et al. 2010; Pope et al. 2006; Greve et al. 2008; Perera et al. 2008; Barger et al. 2008; Wirth et al. 2004). On the other hand, NIR

Table 1. Summary of the MODS observations

field	center position RA	center position Dec	band	exposure time (hour)	FWHM (ch1, ch2) (arcsec)		5σ limit (ch1, ch2)* (Vega mag)	
GT-1	12:36:24.9	+62:10:43	J	8.0	0.59	0.59	24.3	24.2
			H	2.5	0.58	0.59	23.3	23.1
			K_s	8.3	0.58	0.53	23.1	23.2
GT-2	12:36:47.8	+62:13:11	J	28.2	0.48	0.49	25.2	25.2
			H	5.7	0.46	0.46	23.8	23.7
			K_s	28.0	0.45	0.46	24.1	24.1
GT-3	12:37:09.7	+62:15:58	J	6.3	0.57	0.58	24.4	24.3
			H	3.2	0.55	0.55	23.1	23.1
			K_s	10.7	0.59	0.60	23.2	23.2
GT-4	12:37:31.8	+62:18:29	J	9.1	0.58	0.59	24.3	24.3
			H	4.3	0.58	0.59	23.3	23.2
			K_s	9.8	0.59	0.60	23.1	23.1

* the limiting magnitude is estimated from the background fluctuation measured with a aperture diameter of 2 × FWHM of the PSF. The total limiting magnitude for point sources, which is corrected for fluxes missed from the aperture, is ∼ 0.3 mag brighter for each field and band (see text for details).

data which cover the GOODS-North region have reached only $m_{AB} \sim 22$–22.5 (Capak et al. 2004; Bundy et al. 2005), although Wang et al. (2010) recently published relatively deep K_s-band data which reach $K_s \sim 22.7$ (Vega). For J band, there had been no wide-field data which cover most of the GOODS-N region. Therefore NIR data with a comparable depth have been desirable in this field. In this context, with the obtained ultra-deep NIR data, we have investigated the number counts of Distant Red Galaxies at $z \gtrsim 2$ (Kajisawa et al. 2006a), the clustering properties of stellar mass-selected sample at $1 < z < 4$ (Ichikawa et al. 2007), the stellar mass dependence of the X-ray properties of galaxies at $2 < z < 4$ (Yamada et al. 2009), the evolution of the galaxy stellar mass function at $0.5 < z < 3.5$ (Kajisawa et al. 2009), the correlation between the stellar mass and surface brightness for galaxies at $0.3 < z < 3$ (Ichikawa et al. 2010), the relation between the NIR morphology and star formation activity of galaxies at $0.8 < z < 1.2$ (Konishi et al. 2010), the star formation activity as a function of stellar mass at $0.5 < z < 3.5$ (Kajisawa et al. 2010), and the evolution of quiescent galaxies as a function of stellar mass at $0.5 < z < 2.5$ (Kajisawa et al. 2011). Yoshikawa et al. (2010) also used these NIR images with NIR spectroscopic data of star-forming BzK galaxies at $z \sim 2$ to investigate the star formation activity and stellar population of these galaxies.

In this paper, we present the NIR imaging data and a multi-wavelength photometric catalog of K_s-selected sources. Section 2 describes the observations. We give details of the data reduction in Section 3, and the properties of the reduced data in Section 4. In Section 5, we construct the source catalog and explain the catalog entries. Using the source catalog, we present the K_s-band number counts and distribution of NIR colors in Section 6. A summary is presented in Section 7.

The Vega-referred magnitude system is used throughout this paper, unless stated otherwise.

2. Observation

The deep JHK_s-band imaging observations of the GOODS-North were carried out with the Multi-Object InfraRed Camera and Spectrograph (MOIRCS; Ichikawa et al. 2006; Suzuki et al. 2008) on the Subaru Telescope. MOIRCS consists of two 2048 × 2048 HgCdTe HAWAII-2 detectors covering a field of view of 4 × 7 arcmin^2 with a pixel scale of 0.117 arcsec/pixel. Our observations were made on 24 nights (including 8 half nights), in 2006 April-May, 2007 March-May, and 2008 March-May. Figure 1 shows the field layout of the MODS in the GOODS-North region. Four MOIRCS pointings cover a field of ~ 105 (7×15) arcmin^2 (referred to as GT-1 to GT-4 field; see Figure 1). Nominal center positions are shown in Table 1, and adjacent fields overlap by ~ 20 arcsec (Figure 1). The position angle (PA) of the field of view was fixed to 45 degree for most of the observations. Since an engineering-grade chip, which is slightly less sensitive than science-grade one, was used on one of the channels of the MOIRCS (channel-1) in 2008 March-May, however, we also used the PA rotated by 180 degree from the original value (i.e., PA = 225 degree) equally in these observations to equalize the depths of the fields for the both channels. For the K_s-band, we also used archival data of the MOIRCS obtained by other groups, namely, Wang et al. (2009) on 2005 December and 2006 June, and Bundy et al. (2009) on 2006 April.

In the observations, we used the standard circular dithering pattern of the MOIRCS imaging mode (1 center + 8 surrounding pointings) with a diameter of ~ 12 arcsec. The center of the dithering pattern for each sequence was shifted randomly in a 10 arcsec box. Exposure times for each frame in the J, H, and K_s bands are 100–260, 105–180, and 60–210 sec, respectively, which are split into 80–130, 20–40, and 20–70 sec sub-integrations, respectively, to avoid the saturation of the detectors (the co-adding mode). The total integration time for each MOIRCS
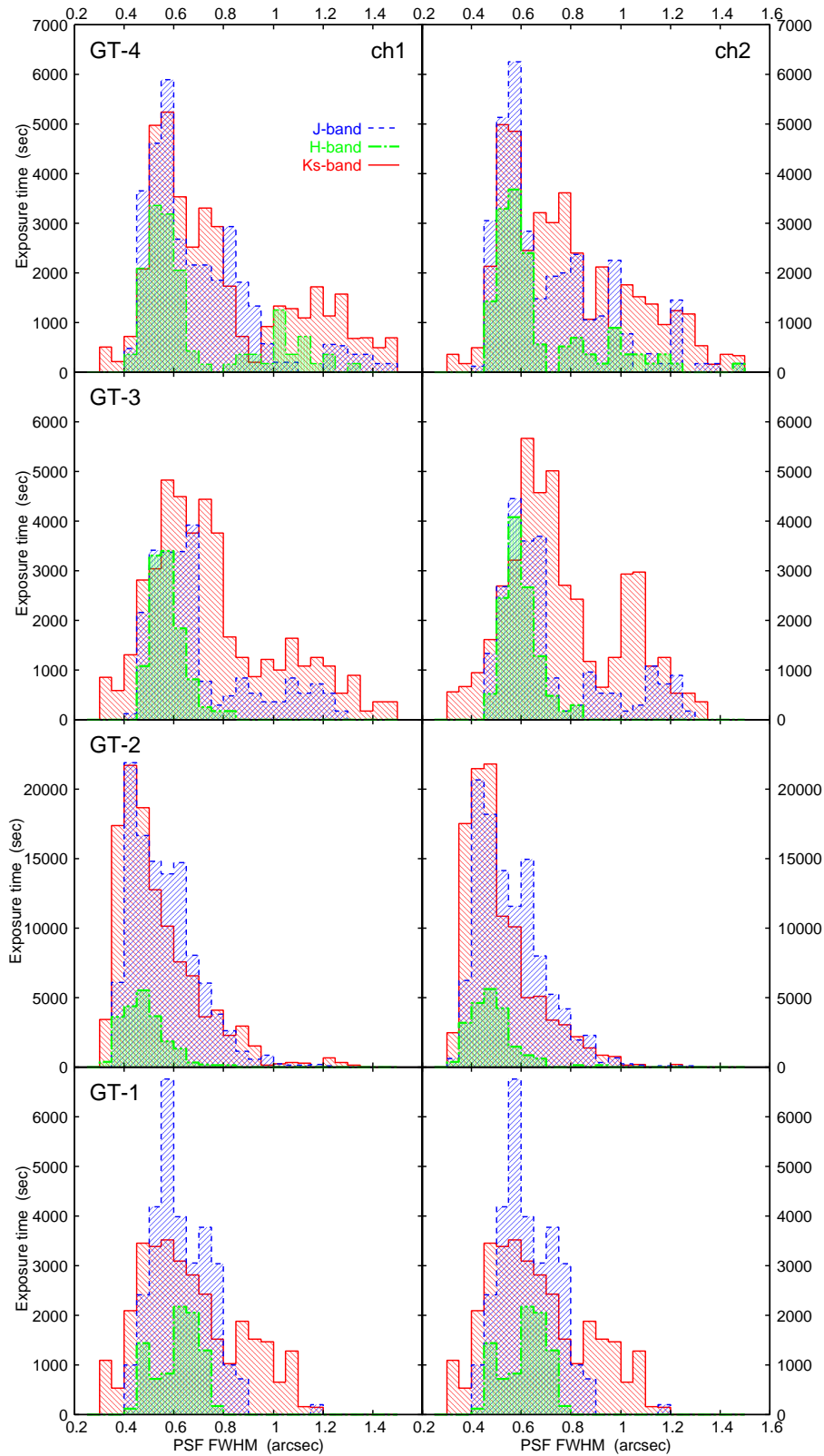
Fig. 2. Distribution of the seeing FWHM of the MODS observations for each field and chip. The seeing was measured with relatively bright isolated point sources in each frame. Blue, green and red histograms show those for J, H and K_s-band data.

pointing is listed in Table 1, and the exposure maps for J, H, and K_s bands are shown in Figure 1. For the GT-1, 3, and 4 fields, the integration times are 6.3–9.1 hours in J band, 2.5-4.3 hours in H band and 8.3-10.7 hours in K_s band, which were adjusted so that the final depth of the survey data is homogeneous. The GT-2 field, which includes the Hubble Deep Field North (HDF-N, Williams et al. 1996; see Figure 1), is the ultra-deep field of the MODS, where the total integration times are longer than the other fields, namely, 28.2 hours in J band, 5.7 hours in H band and 28.0 hours in K_s band.

Figure 2 shows the seeing distribution of the data for each field. We measured FWHM of the point spread function (PSF) for each reduced (before combined) frame using relatively bright isolated point sources. Most of the data were obtained under relatively good seeing conditions ($\lesssim 1.0$ arcsec). In excellent conditions, we preferentially observed the GT-2 field.

A standard star P177-D (Leggett et al. 2006) was observed in a photometric night (1 April 2007) for flux calibration. For the K_s-band data, we used the K-band magnitude of P177-D in Leggett et al. (2006) for the calibration. The difference between K_s and K-band magnitudes for P177-D is negligible. We obtained object frames for flux calibration immediately before the standard star observation at similar airmass in all 4 pointings in JHK_s bands. The total integration time of these object frames for each field and each band is 240–400 sec.

3. Data Reduction

The MOIRCS data were reduced basically using a purpose-made IRAF-based software package called *MCSRED* [1] (Tanaka et al. 2011). The reduction was performed independently for each chip, and then the combined images for the different chips (channel-1 and 2) and fields (GT-1 to GT-4) were mosaiced finally. The basic procedure in the MCSRED is 1) making a quick object mask for each raw frame, 2) making a self-sky flat frame by median stacking of masked raw frames, 3) flat-fielding, 4) making a median sky frame for each flat-fielded frame from 6-8 frames before and after the frame, 5) performing sky subtraction, 6) removing residual sky gradients by fitting each quadrant of the object-masked frame with a 3rd-order polynomial surface and subtracting it from the unmasked image, 7) correcting the optical distortion, 8) measuring positional offsets among the frames and aligning, 9) stacking the frames. Although the self-sky flat for NIR cameras often suffers from thermal emission from the camera, MOIRCS was designed so that the thermal emission from the camera and telescope was minimum (Suzuki et al. 2008). We confirmed that the self-sky flat agrees within 5% with a dome-flat made from the "on − off" frame even in K_s band, where the effect of thermal emission is expected to be maximum. We also checked the photometry at the different positions in the detectors using objects in the overlap regions between the different

chips and fields (see below). Once the reduction sequence was finished, we used the combined image to make a more accurate object mask which includes fainer objects than a quick mask, and then repeated the procedures of 2)–9). Such "second-pass" procedure allows us to remove the effect of faint objects on the flat-fielding and sky subtraction.

In addition to the basic procedure of the *MCSRED*, we also performed a defringing process. Each raw frame obtained in the MODS, which was carried out before the installation of the "fringe-free" type filter, contains a circular fringe pattern produced by the interference of OH air glows. Since the amplitude and center position of the circular pattern varied with time, the fringe pattern cannot be completely removed by the standard sky subtraction procedure. These residual patterns could systematically affect the source detection, photometry, or morphological analysis for objects in the combined images. Figure 3 shows an example of the defringing process for a raw frame (channel-2, K_s-band). The circular fringe pattern can be seen in a frame which is flat-fielded by a dome-flat and is then sky-subtracted with the 3rd-order polynomial surface fitting (top-left panel of the figure). In order to reduce noise and highlight the fringe pattern, we masked objects in the image and convolved the frame with a Gaussian kernel with $\sigma = 2$ pixel (top-middle panel). Then we determined a center of the circular fringe pattern (e.g., yellow curve in the top-middle panel), and converted the image in the Cartesian coordinate system (x, y) to that in the polar coordinate system (r, θ), where the fringe pattern becomes vertical stripes (top-right panel). The converted image was smoothed along the vertical direction (azimuthal direction in the original Cartesian coordinate) with a median filter of 1×401 pixels to reduce noise and fill in the masked region (bottom-right panel). Then the smoothed image was converted back into the Cartesian coordinate system and was multiplied by the dome-flat to obtain a fringe frame for the original raw data (bottom-middle panel). Finally, the fringe frame was subtracted from the raw frame (bottom-left panel).

We used this defringing process twice in the reduction procedure. First, we applied the defringing process to raw data and used the defringed frames to make a sky-flat frame which is not affected by the fringe pattern. With this sky-flat frame, we performed flat-fielding of original (not-defringed) raw data, and then followed the standard sky-subtraction procedures mentioned above. After the sky subtraction, we applied the same defringing process to the sky-subtracted frames to remove the residual of the time-variant fringe pattern. The defringing process after the sky-subtraction has the advantage of much smaller amplitudes of the residual patterns than in a case where the process is directly applied to raw data.

Before the stacking procedure, all object frames were scaled to the count level of the reference frame for the flux calibration mentioned in the previous section, using relatively bright unsaturated sources. We discarded the frames whose count level was less than 70% of the calibration frame, because we often failed in the sky sub-

---

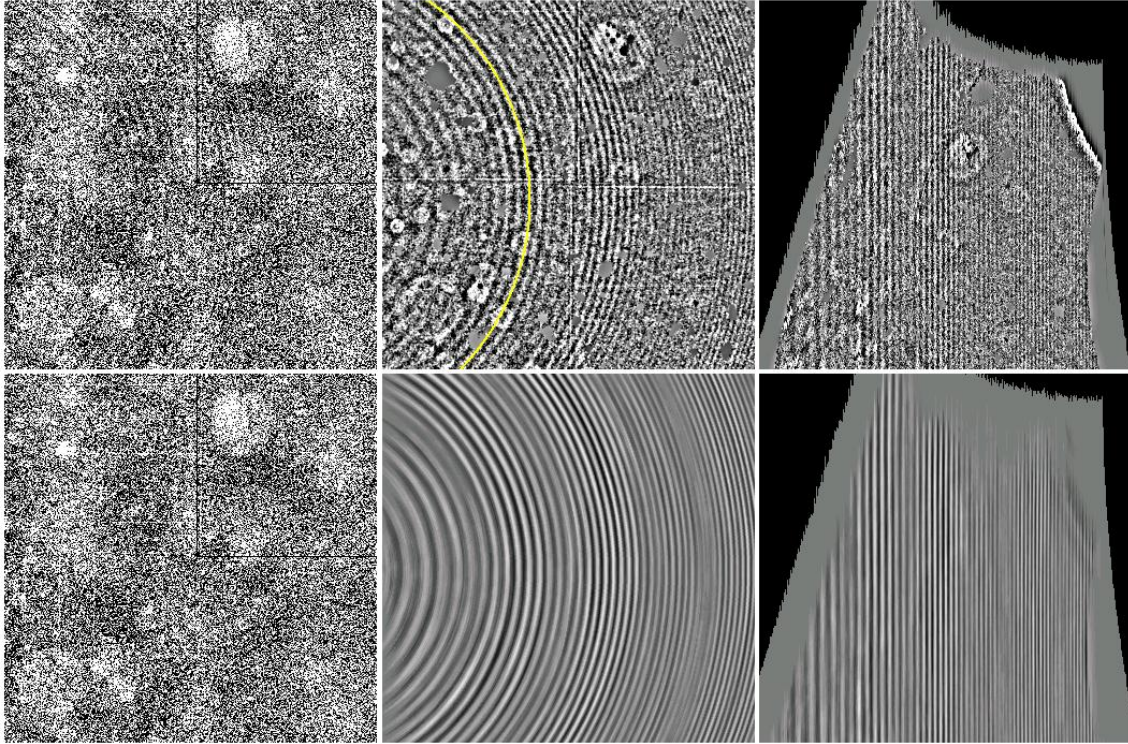[1]   http://www.naoj.org/staff/ichi/MCSRED/mcsred_e.html

Fig. 3. Example of the defringing process for a K_s-band raw frame of channel-2. **top-left:** a raw frame is quick flat-fielded by a dome-flat and sky-subtracted. **top-middle:** objects in the frame is masked and then the frame is convolved with a Gaussian kernel to reduce noise. **top-right:** the frame is converted from Cartesian coordinate system (x, y) to the polar coordinate system (r, θ). **bottom-right:** the converted image is smoothed along the vertical direction with a median filter of 1×401 pixels. **bottom-middle:** the frame is converted back into the Cartesian coordinate system to make a fringe pattern frame. **bottom-left:** the fringe pattern frame is subtracted from the original frame.

traction of these frames due to the bad and unstable sky condition. In the stacking, we used the weighted-average with 3σ clipping. In order to maximize the signal-to-noise (S/N) ratio for the surface brightness of the combined image, each frame was weighted by $1/\sigma_{\mathrm{pix}}^2$, where σ_{pix} is the standard deviation in the pixel-to-pixel statistics of the frame whose count level was scaled to the reference frame. We did not weight the images with seeing size. Instead, we made several combined images for each field and each band using the data sets grouped in different seeing sizes, and measured the background fluctuation of the combined images with apertures of various sizes. Based on the results, we decided to discard frames with a seeing size of FWHM > 1.2 arcsec for the GT-1, 3, and 4 fields and > 0.8 arcsec for the GT-2 field from the stacking. For J and K_s-band data in the GT-2 field, we also provided the high-resolution combined image only from the data sets with a seeing size of < 0.5 arcsec to investigate the morphology of galaxies in the NIR wavelength (Konishi et al. 2010). In addition to the combined image, we also provided the exposure map and RMS map which gives an estimate of the noise level at each pixel. In order to make the RMS map, we first divided the "sigma map" outputted from the IRAF/IMCOMBINE task by the square root image of the exposure map, and then normalized the resulting image so that the average of pixels in the RMS map corresponds to the standard deviation in

the pixel-to-pixel statistics of the combined object image.

In order to mosaic the combined images for the different chips and fields, at first, each combined image was rescaled to a common zero point of 26.0 AB mag (for all JHK_s bands). We then determined the position of each combined image via astrometry using the GOODS HST/ACS version 2.0 data, whose world coordinates agree well with catalogs from the SDSS, 2MASS, and deep VLA 20cm data (Giavalisco et al. 2004; M. Giavalisco and the GOODS Team, 2010, in preparation). Relatively bright isolated stars and galaxies with early-type morphology in each combined image were cross-matched with those in the HST/ACS z_{F850LP}-band image. About 100 such objects were used for each combined image and the world coordinates were determined with a root mean square scatter of $\sim 0.03 - 0.05$ arcsec, which corresponds to $\sim 0.25 - 0.45$ pixels. Based on the determined world coordinates, the combined images were transformed into a common grid of the expanded image of the GT-2 channel-1 data. We performed the photometry of objects in the overlap regions between the different chips and fields to check the zeropoint over the detectors in each band. The magnitudes at the different positions in the detectors agree well and no significant systematic difference is seen. The typical measured average difference and root mean square are 0.03 ± 0.10 mag in J band, 0.02 ± 0.19 mag in H band, and 0.01 ± 0.11 mag in K_s band. In the mosaicing process,

the pixels in the overlap regions of the different images were combined with the weighted-average without sigma clipping. The inverse square of the RMS map for each combined image was used as the weight.

4. Reduced images

4.1. Area coverage

The reduced J, H, K_s-band mosaic images have a pixel scale of 0.117 arcsec and a image size of 4200 × 8400 pixels including the margin. The total exposure times t_{exp} for the images are shorter toward the outer edges as the result of the dithering technique in the observations mentioned above. The area in the J, H, and K_s-band images with $t_{exp} > 3600$ (7200) sec is 106.3 (104.3), 103.3 (98.5), and 118.6 (114.1) arcmin^2, respectively. The larger area coverage in K_s band reflects the contribution from the observations by other groups mentioned above, whose field configurations are different from ours. If we use the homogeneous depth in the central region of each field as a baseline, the area with $\sigma < 2 \times \sigma_{(central\ region)}$ in the RMS maps is 104.6, 104.8, and 109.8 arcmin^2 for the J, H, and K_s-band images. In order to make a K_s-selected source catalog in the next section, we use the area with $t_{exp} > 3600$ sec in the H-band image, which ensures $\sigma < 2 \times \sigma_{(central\ region)}$ in all three bands. The area with $t_{exp} > 3600$ sec in H band is 103.3 arcmin^2 for the whole field and 28.2 arcmin^2 for the deep GT-2 field.

4.2. Image quality and PSF matching

The PSF of the combined image in each chip and field was measured using relatively bright isolated point sources. The FWHMs of the PSF are listed in Table 1. The PSF of the J, H, and K_s-band images for the GT-1, 3, and 4 fields ranges 0.53 – 0.60 arcsec (0.58–0.59 arcsec for the most images). The images for the GT-2 field, which were obtained preferentially in the excellent condition, have sharper PSF with FWHMs of 0.45 – 0.49 arcsec.

Since the different field images have different PSF FWHMs, there is PSF variance in each mosaic image. In order to measure colors of objects with consistent apertures across all bands, we made PSF-matched mosaic images by convolving all images to a common PSF, namely that of the GT-3 K_s-band image, which has the poorest resolution (FWHM = 0.60 arcsec), before the final mosaicing. For the GT-3 J-band and GT-4 K_s-band data, we used the combined images provided from the frames with PSF FWHMs of < 1.0 arcsec for the PSF-matched mosaic images in order to secure a resolution for the proper matching of the PSF to that of the GT-3 K_s-band image. Figure 4 shows a JHK_s-band pseudo-color image made from the PSF-matched mosaic images. We also made PSF-matched mosaic images only for the GT-2 field with a higher resolution. These images were provided from the combined images which were convolved to the resolution of the GT-2 J-band image (FWHM = 0.5 arcsec). In Section 5.2, we compare the growth curve of the point sources in the PSF-matched images among the different bands in order to check the accuracy of the PSF-matching.

4.3. Background noise and limiting magnitude

In order to estimate the background noise and derive the limiting magnitude, we directly measured fluxes of circular apertures placed at random positions on the combined images where objects were masked and replaced with pseudo noise images. In order to provide the pseudo noise images, we averaged 10 randomly-shifted combined images (where objects were masked) and multiplied by the square root of the number of the frames used for the average in each pixel, assuming the Poisson statistics. We then calculated the root mean square of these measurements, and repeated the measurements with various aperture diameters. Figure 5 shows the results for the different chips and fields at each band. For comparison, the expected values from the pixel-to-pixel root mean square scaled by the square root of the aperture area, which is calculated under the assumption that the pixel-to-pixel noise is the Poisson distribution and uncorrelated each other, are also shown in the figure (solid and dashed curves). The empirically measured background noise is larger than that expected from the scaled pixel-to-pixel noise, because adjacent pixels in the combined images become correlated through the reduction procedures such as the distortion correction or the registration of the frames.

We estimated 5σ limiting magnitude for each chip and field using the background fluctuation measured with a aperture diameter of 2 × FWHM of the PSF. These limiting magnitudes are listed in Table 1. For GT-1, 3, and 4 fields, the depth of the data is relatively homogeneous and the limiting magnitudes are $J \sim 24.2$, $H \sim 23.1$, and $K_s \sim 23.1$. In the GT-2 field, the limiting magnitudes are $J \sim 25.1$, $H \sim 23.7$, and $K_s \sim 24.1$, which are ~ 1 magnitude deeper than the GT-1, 3, and 4 fields. In order to derive the total limiting magnitude for point sources, we need to estimate the aperture correction. In Appendix 1, we carry out simulations with the IRAF/ARTDATA package and find that the aperture magnitude with a diameter of 2 × FWHM of the PSF is fainter by ~ 0.28–0.29 mag than the total magnitude for point sources. The total limiting magnitudes for point sources corrected for the missed fluxes are also listed in Table 1.

These limiting magnitudes show that the MODS data are one of the deepest NIR imaging data over a area of ~ 30 to ~ 100 arcmin^2. In particular, the K_s-band data in the GT-2 field is the deepest image obtained to date at the wavelength. For example, the ESO GOODS-South NIR imaging survey with the VLT/ISAAC achieved 5σ limiting magnitudes of $J \sim 24.0$, $H \sim 23.1$, and $K_s \sim 22.5$ over ~ 130 arcmin^2, and the ultra deep K_s-band data with a 5σ limit of $K_s \sim 23.7$ was also obtained over ~ 6.7 arcmin^2 in the HUDF (Retzlaff et al. 2010). The NIR imaging data obtained in the FIRES survey reach 5σ limits of $J \sim 25.3$, $H \sim 24.2$, and $K_s \sim 23.8$ over ~ 4.7 arcmin^2, and $J \sim 24.6$, $H \sim 23.7$, and $K_s \sim 23.1$ over ~ 26.2 arcmin^2 (Labbé et al. 2003; Förster Schreiber et al. 2006). Wang et al. (2010) performed a wider but shallower K_s-band imaging survey than the MODS in the GOODS-North region with the CFHT/WIRCam and achieved a 5σ limit of $K_s \sim 22.7$

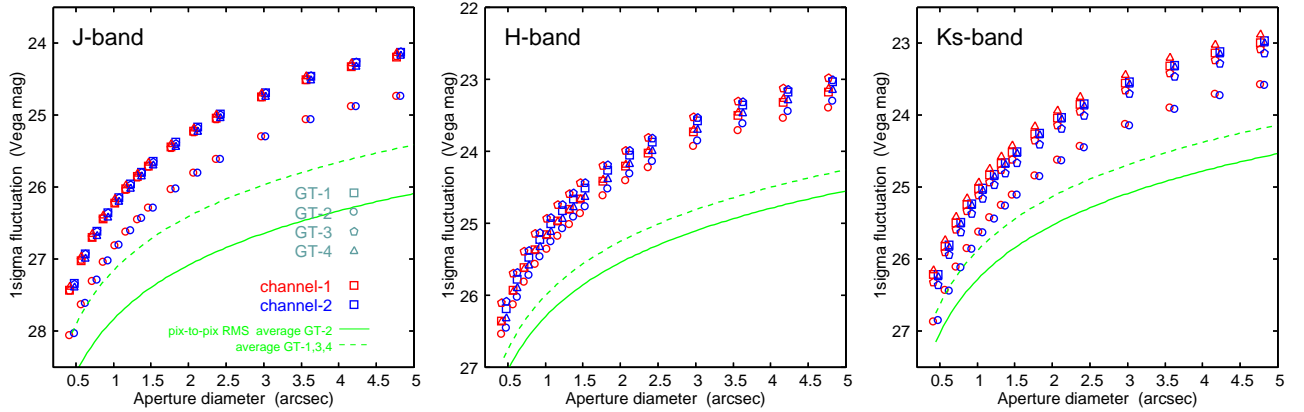**Fig. 4.** JHK_s-band pseudo-color image of the MODS

Fig. 5. Background sky fluctuation as a function of aperture diameter for each band. Different symbols represent the different fields. Red and blue symbols show those for channel-1 and 2, respectively. Dashed and solid lines show the fluctuation expected from the pixel-to-pixel root mean square scaled by the square root of the aperture area under the assumption of the Poisson statistics for the GT-1, 3, and 4 fields and the GT-2 field, respectively.

over ~ 200 arcmin^2.

5. K_s-selected catalog

We constructed multi-band photometric catalogs of K_s-selected sources in the MODS field, using the MODS data and multi-wavelength public data of the GOODS survey, KPNO/MOSAIC U-band data (Capak et al. 2004), HST/ACS B, V, i, and z-band version 2.0 data (Giavalisco et al., in preparation; Giavalisco et al. 2004), and Spitzer/IRAC 3.6, 4.5, 5.8, and 8.0 μm-band DR1 and DR2 data (M. Dickinson et al., in preparation). Two catalogs are provided; one includes objects in the whole MODS field ("wide" catalog), and the other includes only those in the GT-2 field ("deep" catalog). For the deep catalog, the multi-band photometry was performed with a slightly smaller aperture (1.0 arcsec diameter) in the sharper PSF-matched images with FWHM of ~ 0.5 arcsec than that for the wide catalog (1.2 arcsec diameter). It should be noted that the source detection was performed in the K_s-band non-convolved (not PSF-matched) image in both cases. We describe a method of constructing the catalogs and the catalog entries in the following.

5.1. Source detection and completeness

The source detection was performed in the K_s-band image using the SExtractor software version 2.5.0 (Bertin & Arnouts 1996). A detection threshold of 1.3 times the local background root mean square over 12 connected pixels was used. In order to take account of variance of the background noise among different positions in the image, we used the RMS map as a weight image in the source detection procedure. The "local"-type background estimate of the SExtractor was used for the photometry. We adopted MAG_AUTO from the SExtractor as the total K_s-band magnitudes of the detected objects. In Appendix 1, we performed simulations with the IRAF/ARTDATA package to estimate fluxes missed from the Kron apertures of the MAG_AUTO for point sources as a function of K_s-band magnitude. According to the results of the

simulations, the missed fluxes for point sources are expected to be ~ 2–3% at $K \sim 17$–18 mag and become ~ 10–15% near the 5σ limiting magnitudes on average. We also list the magnitude corrected for these average missed fluxes (MAG_AUTO_COR) in the catalogs as well as the original MAG_AUTO. The photometric error for MAG_AUTO was estimated from the background fluctuation shown in Figure 5 measured with a circular aperture whose area is the same as the elliptical Kron aperture used in MAG_AUTO for each object. Since the background noise shown in Figure 5 is averaged over each chip, we also used the RMS map at the object position to take account of the noise variation in each chip and estimate the background noise for the object. Since the RMS map includes an effect of the signal from the objects, we did not add the photon noise from the objects to the photometric error separately.

As mentioned in the previous section, we included only objects with $t_{exp} > 3600$ sec in the H band into the catalogs to ensure relatively uniform depth in JHK_s bands. Total 11660 objects were detected in the selected area of 103.3 arcmin^2. In order to examine the fraction of false detections, we performed a simulation of the source detection on the inverse K_s-band image with the exact same detection parameters. Figure 6 shows number counts of the objects detected in the original image and the false detections expected from the simulation for each chip and field. The 5σ limiting magnitude estimated from the background fluctuation in the previous section is also shown in the figure. The expected false detection rate increases at faint magnitude rapidly, but it is negligible ($\lesssim 1$ %) at brighter than the 5σ limiting magnitude. Below the limiting magnitude ($\lesssim 1$-2σ of the background noise), the numbers of the detections in the inverse image tend to be larger than those in the original image. This may be because the noise property at very faint level is affected by the reduction procedures such as the median sky subtraction.

Around very bright stars, there are also spurious sources caused by the image persistence in the detectors of
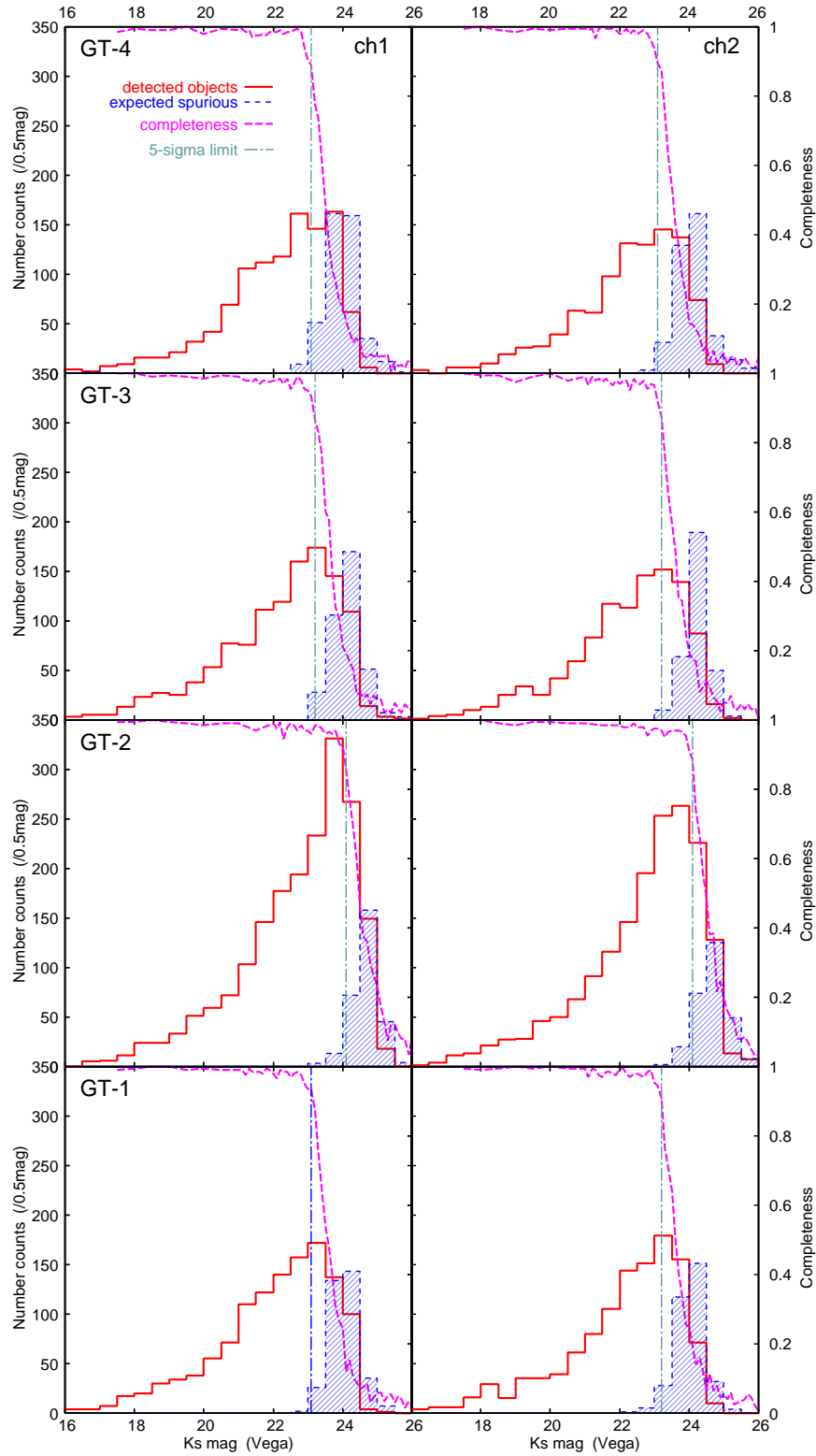
Fig. 6. K_s-band number counts of detected objects (open histogram) and expected false detections (shaded histogram) for each field and chip. Vertical dashed-dotted line in each panel shows the 5σ limiting magnitude. Dashed line shows the detection completeness for the point sources.

MOIRCS. These spurious features are relatively faint and appear at $\sim$ 8–9 arcsec from the bright stars, which corresponds to the dither length between successive positions used in the observations (Section 2). Although we identified 15 spurious sources around very bright stars in the K_s-band image and excluded them from the catalogs, there could remain such spurious sources in the catalogs. Objects near very bright stars should be handled with caution.

We also estimated the detection completeness of our K_s-selected sample using Monte Carlo simulations with the IRAF/ARTDATA package. The detection completeness actually depends on many parameters such as magnitude, size, surface brightness profile, crowdedness, and so on, in a complex way. We here examine the completeness for the point source as a guide. In the simulations, a point source with the corresponding PSF was added at random position in the image. We then ran the SExtractor with the same detection parameters and check whether the added object was detected or not. For each chip and field, 200 such simulations were done for a given magnitude of the point source. The results are shown in Figure 6. The detection completeness for the point sources is $\sim$ 85–90 % level at the 5σ limiting magnitude. The completeness decreases rapidly below the limiting magnitude, and becomes $\sim$ 50 % at 0.5 mag below the limit.

5.2. Color measurements

We measured the optical-to-MIR SEDs of the detected objects, using the U (KPNO/MOSAIC), $BViz$ (HST/ACS), JHK_s (MOIRCS), 3.6, 4.5, 5.8, 8.0 μm (Spitzer/IRAC) -band images. These multi-band images were aligned to the K_s-band mosaic image. We convolved the ACS images with the IRAF/PSFMATCH task to match the PSF-matched images of the MODS. Figure 7 compares the growth curves of the point sources in the PSF-matched images among the different bands (ACS and MOIRCS bands). For the comparison, we made an average PSF from $\sim$ 30 relatively bright, isolated point sources in each PSF-matched image. The growth curves of the stars in the different bands agree within $\pm$ 0.02 mag at radii larger than 0.5 arcsec.

For the color measurements, we basically used a fixed aperture diameter of 1.2 arcsec for the wide catalog and 1.0 arcsec for the deep catalog, respectively, as mentioned above. For MOSAIC (U-band) and IRAC (3.6, 4.5, 5.8, and 8.0 μm-band) data, whose spatial resolution is much poorer than that of the ACS and MOIRCS data, we first performed the aperture photometry for the wide (deep) catalog with aperture sizes of 2.28 (2.39), 2.89 (3.07), 3.05 (3.24), 3.80 (4.02), and 4.10 (4.33) arcsec, respectively, and then applied the aperture correction by using the light profiles of the B- and K_s-band images convolved to match the resolution of U-band and IRAC images, respectively. These aperture sizes for the U-band and IRAC data were selected so that the fraction of the flux sampled by the aperture was the same as that in the ACS and MOIRCS images for point sources. The SExtractor dual-image mode was used for the photometry.

Before running SExtractor, we also performed the subtraction of the contribution from neighboring sources for objects in the crowded region. For the ACS and MOIRCS data, we first picked up all sources in the non-convolved images within 12 arcsec from the K_s-selected object in question. We checked whether the pixel on the K_s-band image at the center position of each picked source belongs to the object in question or not in order to judge if it is the corresponding source. If a picked source did not correspond to the K_s-selected object, this source was extracted from the non-convolved image and then was convolved and subtracted from the PSF-matched (convolved) image. For the U-band and IRAC data, we used the B- and K_s-band images for the subtraction of the contribution from neighboring sources. In this case, all sources picked in the non-convolved B- or K_s-band image were extracted and convolved to match the U-band or IRAC data at first. Then we measured a flux of the central region of the convolved image for each picked source. Here, the central region is defined by the pixels belonging to the source in the non-convolved image. We also measured a flux of the corresponding (central) region in the U-band or IRAC image, and scaled the flux of the convolved B- or K_s-band image to match that in the U-band or IRAC image. This flux scaling was done in order of the brightness of the sources in the U-band or IRAC image. Once the scaling for the brightest source in a crowded region was done, the scaled image was subtracted from the image of the region and then the scaling for the second brightest source was done. After the scaling for all sources finished, the scaled images for sources which do not correspond to the object in question were subtracted from the original U-band or IRAC image.

The error for the aperture photometry was estimated in a similar way with that for MAG_AUTO mentioned above. We measured the background fluctuation for the convolved ACS and MOIRCS data and the MOSAIC and IRAC data with the aperture used in each band, and similarly used a RMS map for each band to estimate the background noise at each object position in the image. When the measured flux for an object is less than 2σ of the background noise, the upper limit is assigned. For objects in crowded regions, we also performed the aperture photometry without the subtraction of the contribution from neighboring sources, and conservatively added a half of the difference between the results with and without the subtraction process to the photometric error.

We included only objects which are detected above 2σ level in more than three bands (K_s band and other two bands) in the main catalogs, because it is difficult to estimate the photometric redshift of those detected only in one or two bands. Of objects detected in the K_s band above 2σ level, 933/10806 and 189/3983 were excluded from the wide and deep catalogs by this criterion. We provide complementary catalogs of these sources separately. Most of these excluded objects are fainter than the 5σ limiting magnitude of the K_s-band data.
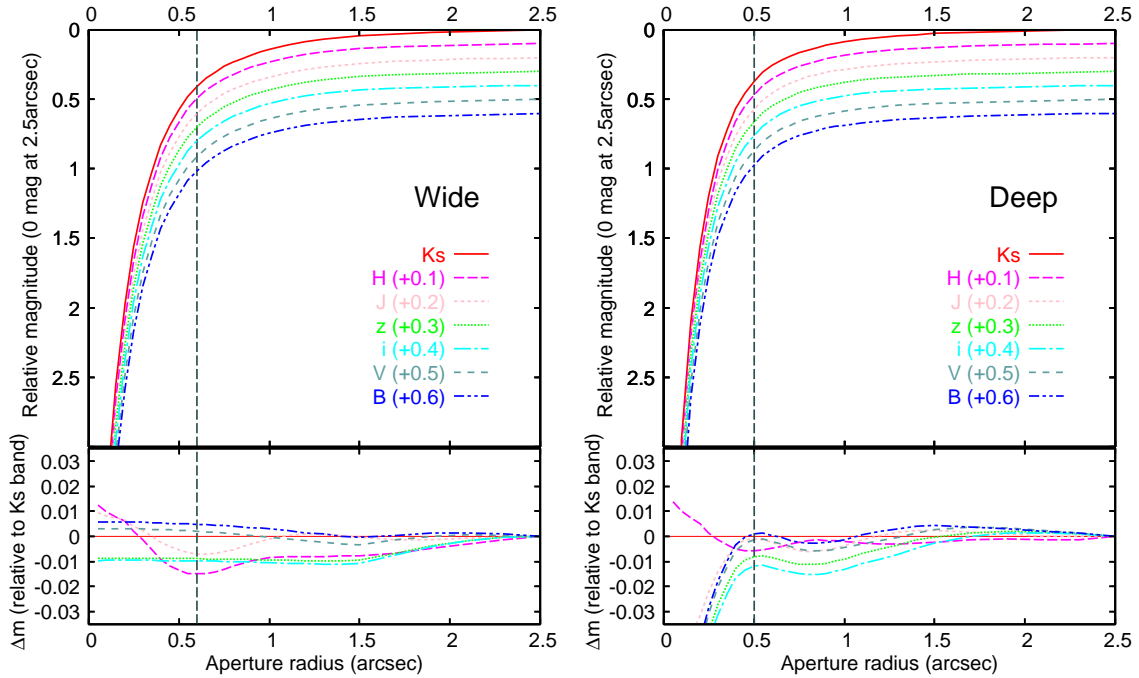
Fig. 7. Comparisons of the growth curves for point sources in the PSF-matched images among the different bands ($BVizJHK_s$) for the wide (left) and deep (right) fields. The growth curves are normalized to 0 mag at 2.5 arcsec radius. The growth curves in the top panels are plotted with vertical offsets (by 0.1 mag) for clarity. The bottom panels show the differences from the K_s band in the growth curves. Vertical long-dashed lines represent the aperture radius used for the color measurements in the wide and deep catalogs.

5.3. Redshifts

Extensive spectroscopic surveys have been carried out in the GOODS-North region. We cross-matched our K_s-selected catalog with spectroscopic catalogs from the literature. We used the catalogs by Yoshikawa et al. (2010), Barger et al. (2008), Reddy et al. (2006), Treu et al. (2005), Wirth et al. (2004), Cowie et al. (2004), Cohen (2001), Cohen et al. (2000), and Dawson et al. (2001). As mentioned above, the World Coordinate System of K_s-band image is based on that of the GOODS HST/ACS ver. 2.0 data, which agrees with these spectroscopic catalogs well. We first identified a pixel on the K_s-band image at the source position in the spectroscopic catalogs, and then found a K_s-selected object to which the pixel belongs. When there were different redshifts from the different catalogs for a K_s-selected object, we chose one from the most recent catalog. Total 2093 K_s-selected objects are assigned spectroscopic redshifts.

For all objects in the wide and deep catalogs, we also estimated the photometric redshift using the $UBVizJHK_s$, 3.6μm, 4.5μm, and 5.8μm-band photometry described in the previous section. We adopted the standard template-fitting technique with population synthesis models. We derived the photometric redshifts with three different population synthesis models, namely, GALAXEV (Bruzual & Charlot 2003), PEGASE version 2 (Fioc & Rocca-Volmerange 1997), and Maraston (2005) model, and also used a public photometric redshift code, EAZY (Brammer et al. 2008) for an independent check of the photometric redshift. The results in all four cases are listed in the

catalogs.

The details of the used templates from each population synthesis model are described in Kajisawa et al. (2009). We here briefly summarize them. We adopted exponentially decaying star formation histories and assumed Salpeter IMF (Salpeter 1955) and Calzetti extinction law (Calzetti et al. 2000) for all three models. Free parameters of the models are age, the star formation timescale τ, dust extinction, and metallicity for the GALAXEV and Maraston models. The model age is changed from 50 Myr to the age of the universe at the observed redshifts, which is calculated for a cosmology with H_0=70 km s^{-1} Mpc^{-1}, $\Omega_m = 0.3$ and $\Omega_\Lambda = 0.7$. For the PEGASE2, we used the same template sets as those used in Grazian et al. (2006), where eight exponentially decaying star formation histories with various gas infalling and star formation timescales are assumed. The metallicity and dust extinction were calculated in the model in a self-consistent way. We also added to the model templates the Lyman series absorption produced by the intergalactic medium following Madau (1995). These model SEDs were compared with the observed multi-band photometry and the minimum χ^2 was found for each object.

Figure 8 compares the photometric redshift with the spectroscopic redshift for objects with spectroscopic identification for the cases with the different population synthesis models. The distribution of δz ($= z_{\rm photo} - z_{\rm spec}$) and the fraction of the catastrophic failure (noted as outliers) with $\delta z/(1+z_{\rm spec}) > 0.5$ are also shown in the figure. The standard deviation of $\delta z/(1+z_{\rm spec})$ is similar among
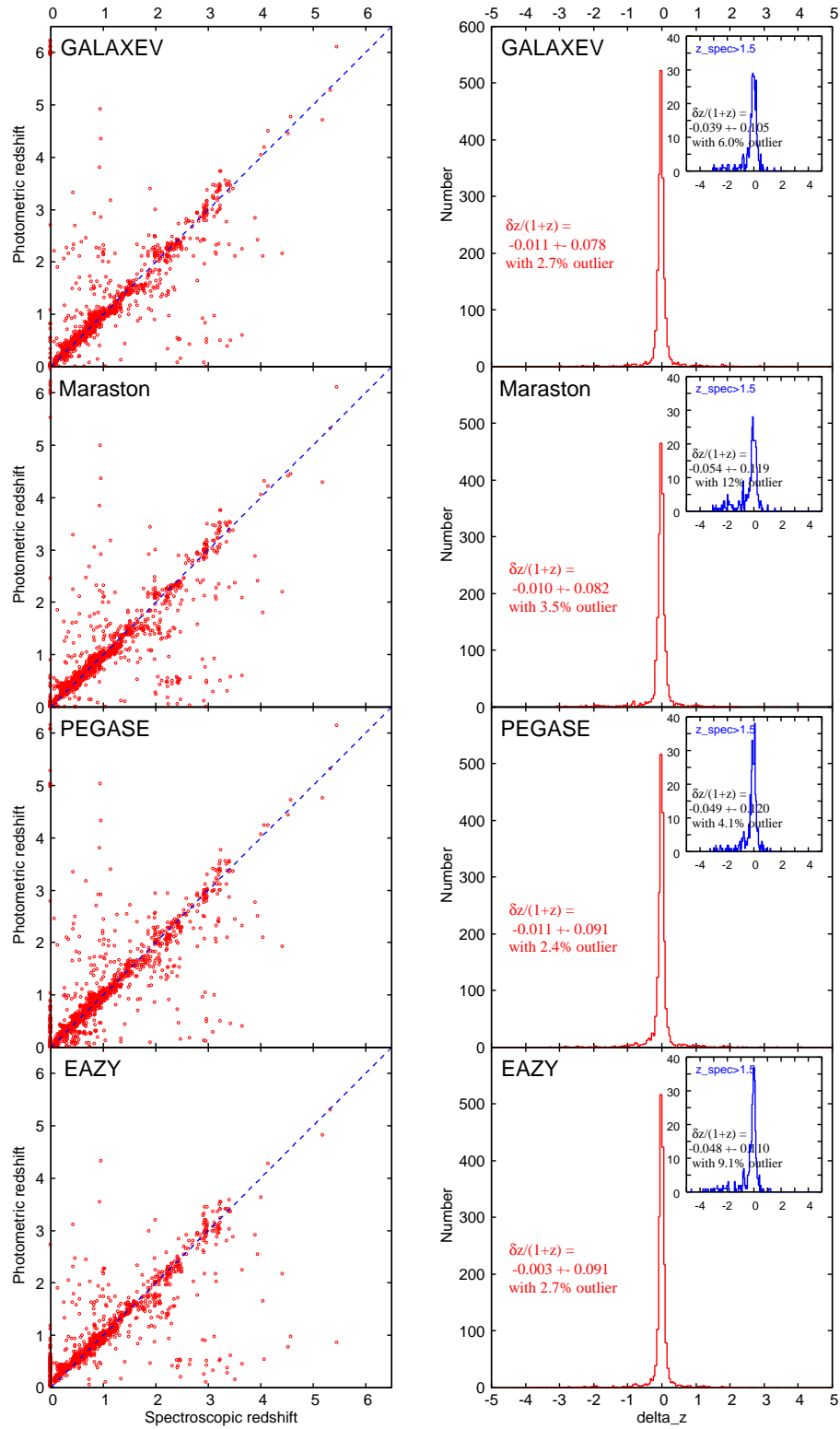
Fig. 8. Comparisons between photometric redshift and spectroscopic redshift for galaxies with spectroscopic redshifts from the literature. The insets in the right panels show those for galaxies with $z_{\rm spec} > 1.5$. The mean difference between the spectroscopic and photometric redshifts and their scatter are also shown.
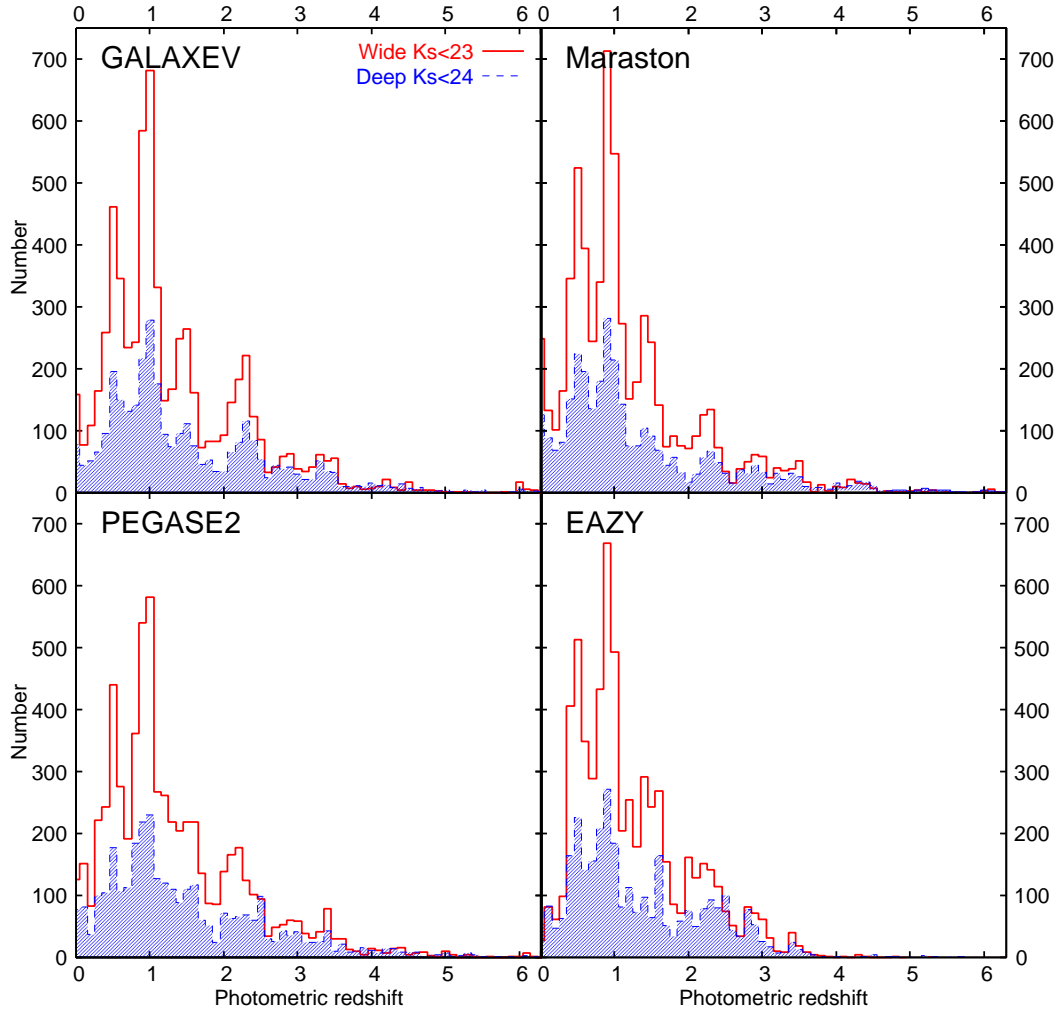
Fig. 9. Photometric redshift distribution for K_s-selected galaxies in the wide (open histogram) and deep (shaded histogram) catalogs. Four panels show the cases where different population synthesis models are used for the photometric redshift.

the cases with the different population synthesis models (~ 0.08–0.09 for all redshift range and ~ 0.11–0.12 for objects at $z_{\rm spec} > 1.5$). Although the photometric redshift accuracy is relatively good in any cases, the fraction of the catastrophic failure at $z > 1.5$ is slightly larger in the case with the Maraston model.

Figure 9 shows the photometric redshift distribution for the cases with the different population synthesis models. In all cases, the distribution shows a primary peak at $z \sim 1$ and a secondary peak at $z \sim 0.5$ and a tail to high redshift. The peaks in the photometric redshift distribution seem to correspond to the large scale structures found by the previous spectroscopic surveys at $z = 0.48$, 0.51, 0.56, 0.85, and 1.02 (Cohen et al. 2000; Wirth et al. 2004). Although the distribution is similar among the cases with the different models, small systematic differences are also seen. In the case with EAZY, for example, the fraction of galaxies in the high redshift tail at $z > 3$ is smaller than the other cases, especially at $z \gtrsim 4$. On the other hand, the number of galaxies at $z \sim 2$–2.5 is slightly small in the case with the Maraston model. These differences seem to occur in the redshift range where the uncertainty of the

photometric redshift is expected to be larger.

5.4. Spitzer/MIPS 24μm fluxes

We measured 24μm fluxes for the K_s-selected objects using public Spitzer/MIPS 24μm data of the GOODS survey (DR1+, M. Dickinson et al., in preparation). As described in Kajisawa et al. (2010), since the source confusion occurs for many objects in the MIPS 24μm data, we used the IRAF/DAOPHOT package (Stetson 1987) for the photometry in order to deal with the blended sources properly, following Le Floc'h et al. (2005). The DAOPHOT software fitted blended sources in a crowded region simultaneously with an PSF, which was empirically constructed from bright isolated point sources in the MIPS image. The source positions in the MOIRCS K_s-band image are used as a prior for the centers of the fitted PSFs in the photometry. The photometric error was calculated from the background noise, which was estimated by measuring sky fluxes at random positions on the MIPS image. After the photometry with the DAOPHOT software, we also performed the aperture photometry for the PSF-subtracted image outputted by the DAOPHOT at
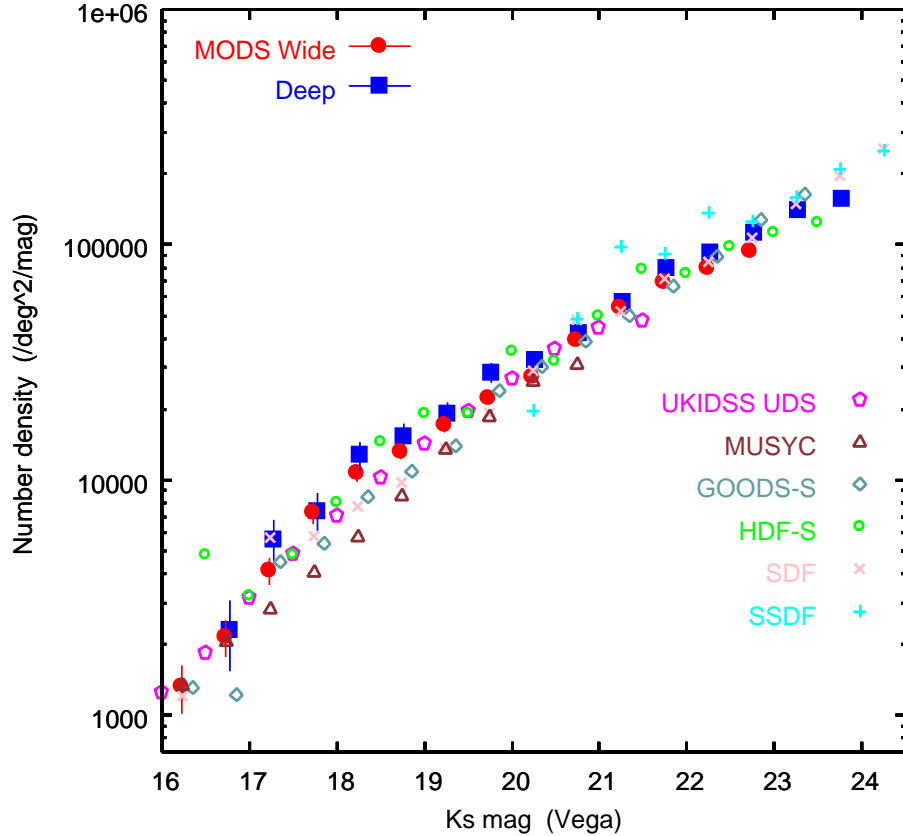
Fig. 10. K_s-band number counts for objects in the MODS field. Solid circles and squares show those for the wide and deep fields. No correction for the incompleteness or false detection is applied for the MODS data. Errorbars are based on the Poisson statistics. Results from other deep NIR surveys are shown for comparison [UKIDSS UDS from Williams et al. (2009), MUSYC from Quadri et al. (2007), GOODS-South from Retzlaff et al. (2010), HDF-South from Labbé et al. (2003), SDF from Maihara et al. (2001), and SSDF from Minowa et al. (2005)].

the same source positions in order to measure the residuals of the PSF fitting. For sources whose fitting residual was larger than the background noise, we added the fitting residual to the photometric error. In the case where the residual of the fitting is negligible, the 5σ limiting flux is ~ 20 μJy.

5.5. Chandra X-ray fluxes

As described in Yamada et al. (2009), we also cross-matched our K_s-selected sample with the X-ray point source catalog of the Chandra Deep Field North (Alexander et al. 2003). The procedure to match the Chandra X-ray source positions in the catalog with the K_s-selected objects was similar with that for the spectroscopic catalogs mentioned above. We identified a pixel on the K_s-band image at the X-ray source position and then found the K_s-selected object to which the pixel belongs. In the case where there is no K_s-band object at the pixel, we extend the search pixels up to three pixel (0.35 arcsec) from the original pixel in order to find the counterpart in the K_s-band image. For most of the Chandra sources, the K_s-band counterparts were actually identified without the extended search thanks to the good positional accuracy of the Chandra data. Thanks to the depth of the K_s-band data, 221 of 226 X-ray sources in the MODS

field from the Alexander et al. (2003)'s catalog have the K_s-band counterparts, and only 5 sources cannot be identified in the K_s-band image. Of these 5 sources, 4 sources are very faint in X-ray and are detected in only one band of the Chandra (full or soft or hard band) at low significance. Therefore these sources might be spurious sources. The other X-ray source is CXOHDFN J123627.5+621218, which is detected in all three bands (full-band flux of 3.7 $\times 10^{-16} erg s^{-1} cm^{-2}$). This source is detected marginally at 3.6 μm and clearly at 4.5 μm, which suggests that this object has a very red SED. For 221 sources with the K_s-band counterparts, the full, soft, and hard-band fluxes are listed in the K_s-selected catalogs.

5.6. Catalog entries

The wide and deep K_s-selected catalogs are publicly available on the MODS web site[2]. It should be noted that all magnitudes in the catalogs are in AB magnitude system. The conversion from the Vega system to the AB system in the MOIRCS JHK_s bands are $J_{AB} = J_{Vega} + 0.915$, $H_{AB} = H_{Vega} + 1.354$, and $K_{sAB} = K_{sVega} + 1.834$, respectively. The catalog entries are as follows.

- ID — sequential identification number in order

---
[2]   http://www.astr.tohoku.ac.jp/MODS/

Table 2. K_s-band number counts for the wide and deep fields. Errors of the number density are based on the Poisson statistics.

K_s mag (Vega)	Wide (103.3 arcmin^2)			Deep (28.2 arcmin^2)		
	Number	Number density (deg^{-2} mag^{-1})	error (deg^{-2} mag^{-1})	Number	Number density (deg^{-2} mag^{-1})	error (deg^{-2} mag^{-1})
16.25	19	1223.9	303.7	1	255.0	255.0
16.75	31	2160.0	387.9	9	2295.0	765.0
17.25	59	4111.0	535.2	22	5610.1	1196.1
17.75	104	7246.5	710.6	29	7395.1	1373.2
18.25	154	10730.4	864.7	50	12750.1	1803.1
18.75	190	13238.8	960.4	60	15300.2	1975.2
19.25	245	17071.0	1090.6	75	19125.2	2208.4
19.75	320	22296.8	1246.4	112	28560.3	2698.7
20.25	391	27244.0	1377.8	127	32385.3	2873.7
20.75	565	39367.9	1656.2	164	41820.4	3265.6
21.25	777	54139.5	1942.2	225	57375.6	3825.0
21.75	999	69608.0	2202.3	311	79305.8	4497.0
22.25	1137	79223.5	2349.5	362	92311.0	4851.8
22.75	1346	93786.1	2556.3	438	111691.2	5336.8
23.25				550	140251.5	5980.3
23.75				614	156571.6	6318.7

as outputted by SExtractor. IDs in the wide and deep catalogs are independently assigned (see ID_[deep/wide] below).

- X_PIXEL, Y_PIXEL — pixel coordinates in the mosaiced K_s-band image.
- RA, Dec — right ascension and declination coordinates (J2000), which are based on the GOODS HST/ACS ver. 2.0 data.
- K_AUTO — K_s-band Kron magnitude (MAG_AUTO from SExtractor) in AB magnitude.
- K_AUTO_COR — K_s-band Kron magnitude corrected for fluxes missed from the Kron aperture (assuming the surface brightness profile of point sources, see Section 5.1 and Appendix 1 for details).
- SNR_AUTO — signal to noise ratio for the K_s-band Kron magnitude.
- rad_AUTO — aperture radius used for the K_s-band Kron magnitude (2.5 × Kron radius) in pixel unit. The circularized value is listed.
- rad_half — K_s-band circularized half light radius in pixel unit.
- flag — extraction flags from SExtractor
- {UBVizJHKs, 3.6, 4.5, 5.8, 8.0}_ap — aperture magnitude in AB magnitude in each band. The aperture with 1.2 (1.0) arcsec diameter is basically used for the wide (deep) catalog.
- {UBVizJHKs, 3.6, 4.5, 5.8, 8.0}_err — photometric error for the aperture magnitude in each band. Negative error indicates that the aperture magnitude is the 2σ upper limit.
- f_24um, err_24um — MIPS 24μm flux in μJy and associated error.
- flux_X, flux_XSB, flux_XHB — Chandra X-ray fluxes in full, soft, and hard bands, respectively, in erg s^{-1} cm^{-2}.

- z_spec — spectroscopic redshift from the literature.
- refer_spec — reference for the spectroscopic redshift. 1: Yoshikawa et al. (2010), 2: Barger et al. (2008), 3: Reddy et al. (2006), 5: Treu et al. (2005), 6: Wirth et al. (2004), 7: Cowie et al. (2004), 8: Cohen (2001), 9: Cohen et al. (2000), 10: Dawson et al. (2001).
- IDref_spec — ID in the spectroscopic catalog.
- zph_BC, zph_MR, zph_PG — photometric redshifts with the population synthesis models of GALAXEV, Maraston, and PEGASE2.
- zph_EZ — photometric redshift outputted by EAZY.
- wht_{UBViz} — weight value (inverse variance per pixel) at the object position in each band.
- exp_{JHKs, 3.6, 4.5, 5.8, 8.0} — exposure time at the object position in seconds in each band.
- exp_24um — exposure time at the object position in seconds in the MIPS 24μm image.
- exp_{X, XSB, XHB} — effective exposure time at the object position in seconds in the Chandra full, soft, and hard-band images, respectively.
- ID_deep, ID_wide — ID of the corresponding object in the other (deep or wide) catalog.

6. Analysis

We here present the K_s-band number counts and distribution of NIR colors, and demonstrate some selection techniques with the NIR colors for high redshift galaxies. In appendix 2, we also compare the K_s-band total magnitude and colors between the K_s band and the other U-to-8.0μm bands in the MODS catalogs with those in other studies to check our photometry.

6.1. K_s-band Number Counts

Using the K_s-selected catalogs described above, we constructed K_s-band number counts. Figure 10 and Table 2 show the number counts for objects in the wide and deep fields. We limited the samples to $K_s < 23$ ($K_s < 24$) for objects in the wide (deep) field, where the detection completeness is very high ($\gtrsim 90\%$ at least for point sources) and the spurious detection is negligible as seen in Figure 6. No correction for the incompleteness or the false detection is applied. The number counts are calculated in 0.5 mag bins and error bars are based on Poisson statistics. For comparison, those of other deep NIR surveys, namely, the UKIDSS UDS with UKIRT/WFCAM (Williams et al. 2009), the MUSYC deep NIR fields with CTIO 4m/ISPI (Quadri et al. 2007), the GOODS-South with VLT/ISAAC (Retzlaff et al. 2010), the FIRES HDF-South with VLT/ISAAC (Labbé et al. 2003), Subaru Deep Field (SDF) with Subaru/CISCO (Maihara et al. 2001), and Subaru Super Deep Field (SSDF) with Subaru/IRCS+AO (Minowa et al. 2005), are also shown in the figure. K_s-band counts of the MODS agree well with the results of other surveys especially at faint magnitudes. The MODS number counts are slightly higher than those of other surveys at $K_s \sim 18$–19 and it is also seen that the number counts in the MODS deep field is sightly higher than those in the wide field. These might be due to the large scale structures around the HDF-N (Cohen et al. 2000; Wirth et al. 2004) which the GT-2 field includes as mentioned above.

The logarithmic slope $d(\log N)/dm$ of the MODS number counts seems to decrease with magnitude. For example, the best-fit slope to the number counts at $20 < K_s < 24$ is $\alpha = 0.20 \pm 0.04$, while the slope becomes steeper at $K_s \lesssim 18$. The change in the logarithmic slope of the K-band counts at $K \sim 17$–18 has been reported by previous studies (e.g., Cristóbal-Hornillos et al. 2003; Cristóbal-Hornillos et al. 2009; Quadri et al. 2007). The slope at the faint magnitude of $K_s > 20$ is consistent with the results of the FIRES survey (Labbé et al. 2003; Förster Schreiber et al. 2006), although it is slightly flatter than those of the GOODS-S and SDF (Retzlaff et al. 2010; Maihara et al. 2001). If we divide the sample at $K_s \sim 21$ and estimate the slope of the number counts separately, the slope is $\alpha = 0.22 \pm 0.06$ at $18 < K_s < 21$ and $\alpha = 0.18 \pm 0.05$ at $21 < K_s < 24$. Although the uncertainty is rather large, the flattening of the slope with magnitude may continue even at $K \gtrsim 19$.

6.2. NIR Color distribution

Figure 11 shows $J - K_s$ vs. K_s color-magnitude diagram for objects with $K_s < 23$ in the wide field and those with $23 < K_s < 24$ in the deep field. Spectroscopically confirmed stars are shown as squares in the figure. These stars form a upper envelope at $J - K_s \sim 0.9$ in their color-magnitude distribution, which is consistent with the expected locus of Galactic stars. Objects with S/N < 2 in J band are plotted at their 2σ lower limit of the $J - K_s$ color as symbols with arrows. Thanks to our deep J-band data
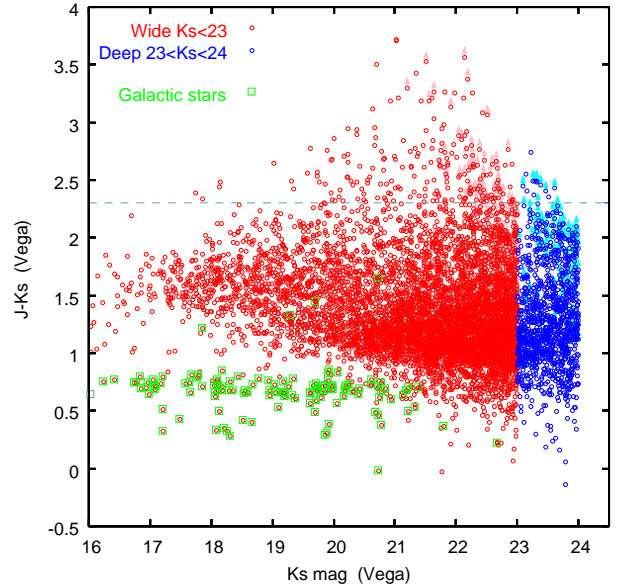

Fig. 11. $J - K_s$ vs. K_s color-magnitude diagram for objects in the MODS field. Red circles show objects with $K_s < 23$ in the wide field, while blue ones show objects with $23 < K_s < 24$ in the deep field. Objects with S/N < 2 in J band are plotted at their 2σ lower limit of the $J - K_s$ color with arrows. Open squares represent spectroscopically confirmed Galactic stars. Horizontal dashed line shows $J - K_s = 2.3$, which is used as for the DRG selection.

(the 2σ limit of $J \sim 25.2$ for the wide field and $J \sim 26.1$ for the deep field), we can do the color measurement up to rather red $J - K_s$ colors. For example, we can measure objects with $J - K_s \sim 3$ down to $K_s \sim 22.2$ ($K_s \sim 23.1$) for the wide (deep) field. The dashed line in the figure represents $J - K_s = 2.3$, which is used as the limit for the Distant Red Galaxies (DRGs, Franx et al. 2003). We can select DRGs with $J - K_s > 2.3$ down to $K_s \sim 22.9$ for the wide field and $K_s \sim 23.8$ for the deep field, and detected 208 DRGs in the wide field and 81 DRGs in the deep field (65 are overlapping). Figure 12 shows the distribution of the K_s-band magnitude and redshift for the DRGs. In the figure, we used the spectroscopic redshifts (18 galaxies) if available, otherwise the photometric redshifts with the GALAXEV model. The K_s-band number counts of the DRGs seem to turnover at $K_s \sim 22$ and do not increase with magnitude at $K_s \gtrsim 22$ as found in Kajisawa et al. (2006a). The DRGs lie mainly at $2 \lesssim z \lesssim 3.5$, and there are tails in the redshift distribution at $z \sim 0.5$–2 and $z \sim 3.5$–4.5, which is consistent with the results of other deep surveys (e.g., Förster Schreiber et al. 2006; Quadri et al. 2007; Quadri et al. 2008). At low redshift ($z \lesssim 2$), the number of DRGs does not increase with magnitude, and that of faint DRGs is relatively small. A similar trend is also seen at higher redshift in the magnitude range we investigated. On the other hand, the brightest K_s-band magnitude of the DRGs at each redshift gradually shifts to fainter values with redshift. As a result, the redshift distribution of the DRGs shifts to higher redshift with K_s-band magnitude. The DRGs at relatively low redshift dominate at bright magnitude ($K_s \lesssim 19$), which is also
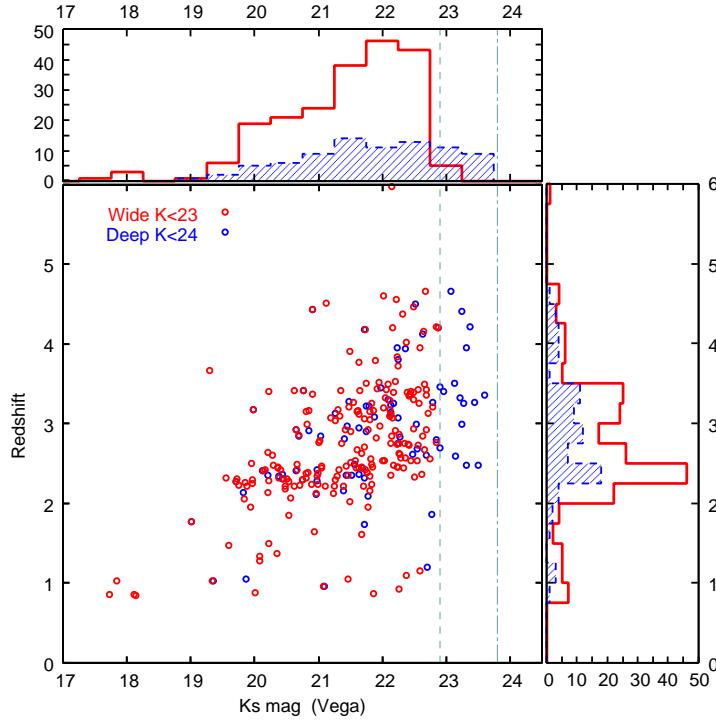
Fig. 12. Redshift vs. K_s-band magnitude for DRGs in the MODS field. Red symbols show DRGs with $K_s < 23$ in the wide field, while blue symbols represent DRGs with $K_s < 24$ in the deep field. Upper panel shows the K_s-band number counts of the DRGs, and right panel shows the redshift distribution of these objects. Vertical dashed and dotted-dashed lines represent the K_s-band limit for the DRGs in the wide and deep fields, respectively.
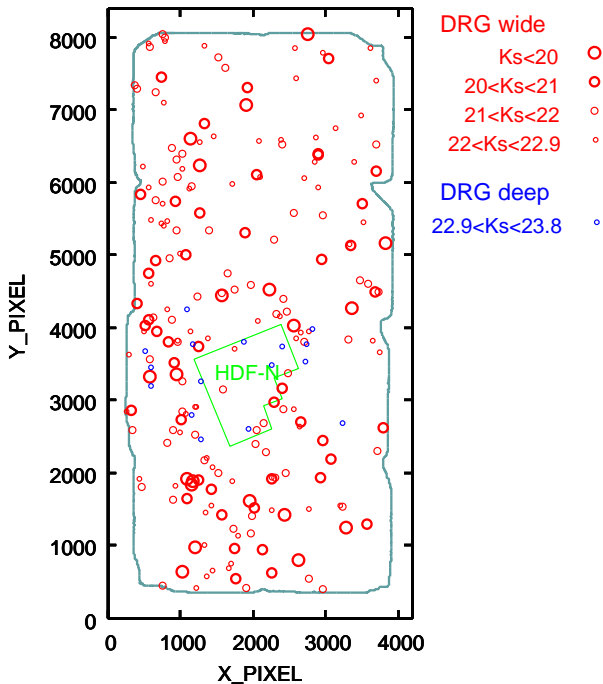

Fig. 13. Spatial distribution of DRGs in the MODS field. The size of the symbols is scaled according to apparent magnitudes in the K_s-band. Red symbols show the DRGs with $K_s < 22.9$ in the wide field, while blue symbols represent those with $22.9 < K_s < 23.8$ in the deep field. Thick solid line shows the survey area for which our catalog was constructed ($t_{exp} > 3600$ sec in the H-band). The original HDF-N field is also shown as thin line.

consistent with the result of Conselice et al. (2007).

Figure 13 shows the spatial distribution of the DRGs in the MODS field. As found by Ichikawa et al. (2007) for those in the GT-2 field, these DRGs seem to be strongly clustered. For example, several bright DRGs concentrate at (X∼1200, Y∼1900). One of these galaxies has $z_{\rm spec} = 3.661$, while five of the other six DRGs show $z_{\rm phot} = 2.2$–2.5 (the other one has $z_{\rm phot} \sim 1.3$). On the other hand, there are few bright DRGs in the original HDF-N field as shown in Kajisawa et al. (2006a). At ~ 2.5 arcmin scale (~ 1300 pixels), there are other similar voids of bright DRGs in the MODS field. The field-to-field variance of the number density of these galaxies seems to be large at the scale.

The left panel of Figure 14 shows $J - K_s$ vs. $H - K_s$ color-color diagram for objects with $K_s < 23$ in the MODS field. We show only objects with S/N > 2 in H band in the figure. Again, squares represent the spectroscopically confirmed stars. They lie mainly at $0.3 \lesssim J - K_s \lesssim 0.9$ and $0 \lesssim H - K_s \lesssim 0.3$, and there are also some red stars. Their distribution in the color-color diagram is consistent with that expected for Galactic stars, which indicates that the zero points of our J, H, and K_s-band data have been correctly determined. The distribution of galaxies in the $J - K_s$ vs. $H - K_s$ diagram is also consistent with those seen in other NIR surveys (e.g., Förster Schreiber et al. 2006; Retzlaff et al. 2010). For an example of a color selection technique for high-redshift galaxies in the color-color diagram, we show the selection criterion for Balmer break galaxies at $z \sim 2.5$ introduced by Kajisawa et al. (2006b)
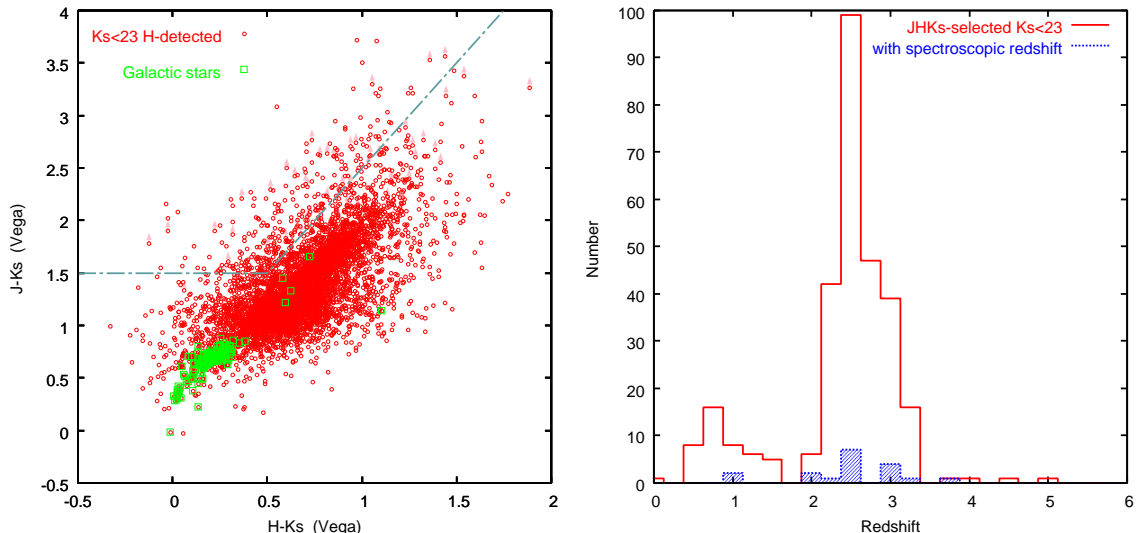
Fig. 14. left: $J - K_s$ vs. $H - K_s$ two-color diagram for objects in the MODS field. Only objects with $K_s < 23$ and S/N > 2 in H band located in the wide field which are detected in H band are plotted. Objects with S/N < 2 in J band are plotted at their 2σ lower limit of the $J - K_s$ color with arrows. Open squares show spectroscopically confirmed stars. Dashed-dotted line represents the selection criterion for Balmer break galaxies at $z \sim 2.5$ introduced by Kajisawa et al. (2006b), namely, $J - K_s > 2(H - K_s) + 0.5$ and $J - K_s > 1.5$. **right:** Redshift distribution of the Balmer break galaxies selected by the JHK_s color criterion. Open histogram shows all selected objects with $K_s < 23$, and shaded histogram shows those with spectroscopic identification.

in the left panel of Figure 14 (dotted-dashed line). This criterion is $J - K_s > 2(H - K_s) + 0.5$ and $J - K_s > 1.5$, and is met while the Balmer/4000 Å break of galaxies falls between J and H bands (i.e., $2 \lesssim z \lesssim 3$), whereas most of the foreground and background galaxies would not meet such a criterion. The right panel of Figure 14 shows the redshift distribution of objects selected by this criterion. Again we used the spectroscopic redshifts if available, otherwise the photometric ones with the GALAXEV model. Most of these galaxies lie at $2 \lesssim z \lesssim 3.2$ showing a strong peak at $z \sim 2.5$, although there is a relatively small contamination ($\sim 15\%$) from low-redshift galaxies. Thus, the deep JHK_s-band data of the MODS allow us to sample the SEDs around the Balmer/4000 Å break of galaxies at $2 \lesssim z \lesssim 3$ with high accuracy, which is important for investigating the stellar population of these high-redshift galaxies.

7. Summary

In this paper, we presented the deep JHK_s-band imaging data of the MODS obtained with MOIRCS on the Subaru telescope. The data cover an area of 103.3 arcmin^2 in the GOODS-North region and reach the 5σ total limiting magnitudes for point sources of $J = 23.9$, $H = 22.8$, and $K_s = 22.8$. In 28.2 arcmin^2 of the survey area, the data reach the 5σ depths of $J = 24.8$, $H = 23.4$, $K_s = 23.8$. The World Coordinate System of the reduced images is based on the public HST/ACS ver. 2.0 data of the GOODS. The image quality of the combined images is characterized by a PSF with FWHM of ~ 0.53–0.60 arcsec for the wide field and ~ 0.45–0.49 arcsec for the deep field, respectively. For the color measurements, we also provided the PSF-matched mosaic images whose FWHM of the PSFs

are 0.6 arcsec for the wide field and 0.5 arcsec for the deep field. The K_s-band detection completeness for the point sources is $\sim 90\%$ at $K_s \sim 23$ for the wide field and at $K_s \sim 24$ for the deep field. The spurious sources are also negligible down to these completeness limits, although the false detection rate increases rapidly below the limits.

Combining the multi-wavelength public data taken with the HST, Spitzer, and other ground-based telescopes in the GOODS field with the MODS data, we constructed the multi-wavelength photometric catalogs of K_s-selected sources. Total 9875 and 3787 objects are listed in the wide and deep catalogs. The catalogs also include the Spitzer/MIPS 24 μm fluxes, Chandra X-ray fluxes, and redshifts of the K_s-selected objects. The comparisons between the spectroscopic and photometric redshifts suggest that the photometric redshift accuracy is $\delta z/(1 + z_{\rm spec}) \lesssim 0.1$ with $\sim 3\%$ outliers for galaxies with spectroscopic redshifts (~ 4–12% outliers for objects with $z_{\rm spec} > 1.5$).

Using the catalogs, we examined the K_s-band number counts and NIR color distribution. The K_s-band number counts in the MODS field are consistent with those in other general fields and show the logarithmic slope of $d(\log N)/dm \sim 0.2$ at $K \gtrsim 20$. The NIR color distribution of spectroscopically confirmed stars indicates that the zero points of the MODS data have been correctly determined. We also demonstrated some selection techniques for high-redshift galaxies with the NIR colors.

The MODS data are one of the deepest NIR imaging data over a area of ~ 30 to ~ 100 arcmin^2 to date, especially in the K_s band. These data sample an important part of the SEDs of galaxies at $1 \lesssim z \lesssim 4$ to study their stellar population. The high image quality of the data is very useful for the deconvolution of other imaging data with poorer spatial resolution, while their

depth in the NIR is essential for the identification of objects detected in the multi-wavelength data, which have been obtained by the Chandra, Spitzer, Herschel, VLA, and so on. These imaging data and K_s-selected source catalogs are publicly available on the MODS web site (http://www.astr.tohoku.ac.jp/MODS/).

Appendix 1. Simulations for estimating the aperture corrections

In this section, we investigate how the MAG_AUTO from SExtractor misses fluxes as a function of magnitude, using simulations with the IRAF/ARTDATA package. Although such aperture correction could depend on not only magnitude but also size, surface brightness profile, and morphology of objects, we here examine the aperture correction for point sources as a guide. The aperture correction for point sources can be considered to be the minimum correction. The procedures are the same as in the measurement of the detection completeness in Section 5.1. An artificial point source with the corresponding PSF was added at random position in the K_s-band image of each chip and field. We then ran the SExtractor with the same detection parameters and compared the input magnitude and the output MAG_AUTO. The results are shown in Figure 15. The MAG_AUTO is fainter by $\sim$ 0.02–0.03 mag than the input total magnitude at $K \sim$ 17–18 and becomes fainter by $\sim$ 0.15 mag near the 5σ limiting magnitude ($K \sim 23$ for the GT-1, 3, and 4 fields, and $K \sim 24$ for the GT-2 fields). The aperture correction seems to be slightly smaller for the GT-2 field data, which is ~ 1 mag deeper and has higher image quality. We fitted the difference between the input total magnitude and the output MAG_AUTO (i.e., the aperture correction) as
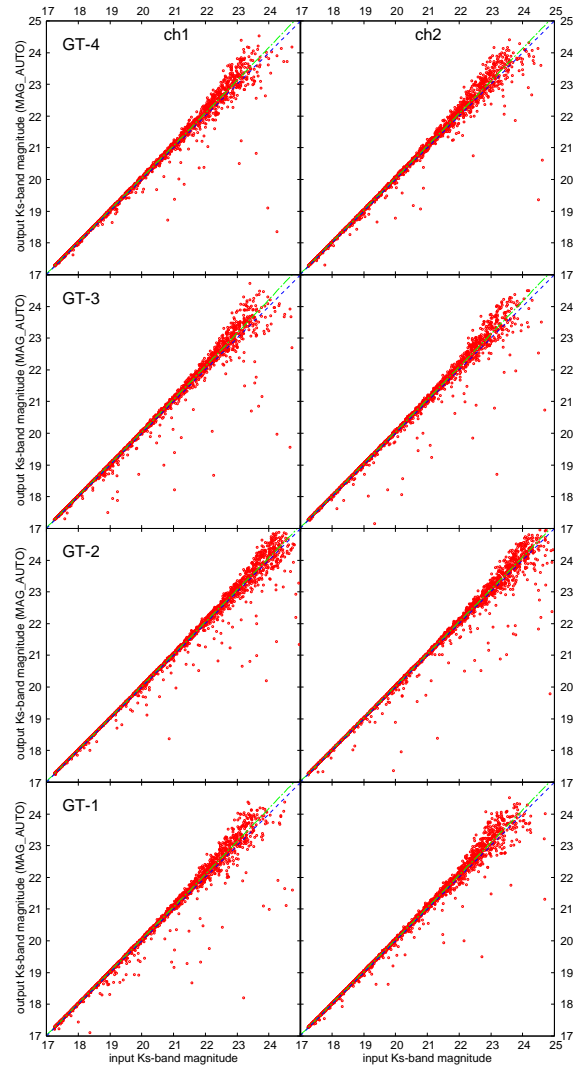

Fig. 15. Comparison between the input K_s-band total magnitude and the measured MAG_AUTO for artificial point sources in the simulations for each chip and field. Dotted-dashed line shows the best-fit second-order polynomial function.

a function of the *measured* MAG_AUTO with a second-order polynomial function. We used the results to correct the MAG_AUTO and listed the corrected MAG_AUTO as MAG_AUTO_COR in our catalogs (Section 5.6).

In the simulations, we also measured the aperture magnitude for the artificial point sources with a aperture diameter of $2 \times$ FWHM of the PSF to estimate the aperture correction for the limiting magnitude measured with the aperture in Section 5.1. Figure 16 compares the aperture magnitude measured with the $2 \times$ FWHM diameter with the input total magnitude. The difference between these two magnitudes is nearly constant over a wide range of the magnitude, especially at bright magnitude. We fitted the difference at the input $K_s < 20$, assuming that it is constant over magnitude. The resulting aperture correction is similar among the different chips and fields and is ~ 0.28–0.29 mag. The total limiting magnitudes for point sources are expected to be brighter by these values than
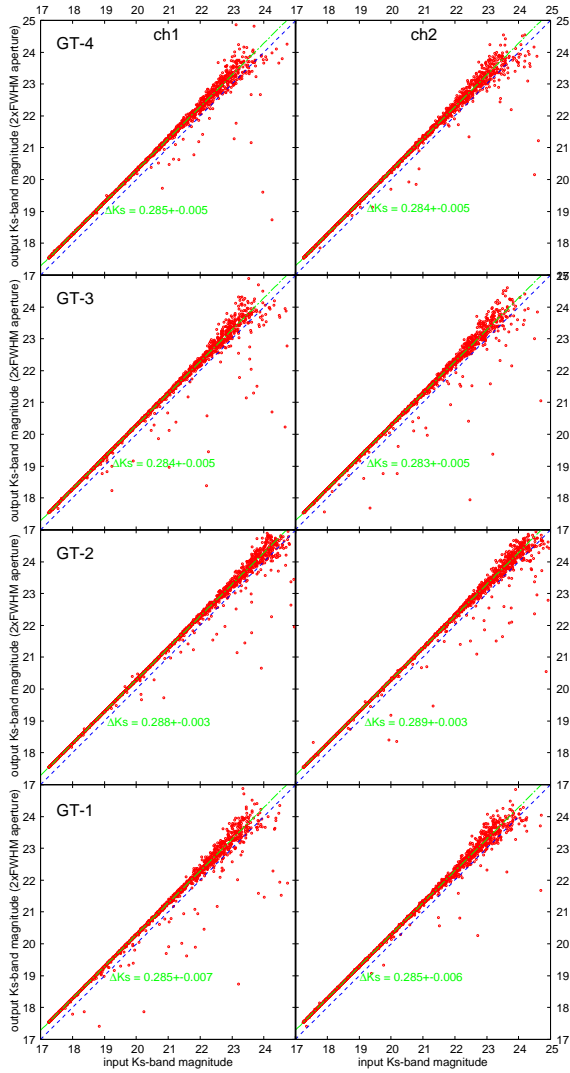
Fig. 16. Comparison between the input K_s-band total magnitude and the aperture magnitude measured with a aperture diameter of $2 \times$ FWHM of the PSF in the simulations for each chip and field. Dotted-dashed line represents the result of the linear fitting for the data at $K_s < 20$.

those estimated from the background fluctuation which was measured with a aperture diameter of $2 \times$ FWHM. The corrected limiting magnitudes for point sources are also listed in Table 1.

Appendix 2.   Comparison of the photometry with other studies in the GOODS-North

In order to check the photometric accuracy, we here compare the K_s-band total magnitude and colors between the K_s band and the other U-to-8.0μm bands in our catalogs with other studies in the GOODS-North field. The procedure to match sources in the catalogs of other studies with those in the MODS catalog is the same as that for the spectroscopic catalogs (Section 5.3). We excluded objects with the deblended flag (from SExtractor) in our catalog from the comparisons in order to avoid the effects of the different spatial resolution of the images used in the

different studies on the source detection.

Figure 17 compares the K_s-band total magnitudes in the MODS catalog with those in Barger et al. (2008) and Bundy et al. (2009). We here used the original (not aperture-corrected) MAG_AUTO for direct comparisons with these studies. Barger et al. (2008) obtained deep K_s-band data with CFHT/WIRCam and calibrated the WIRCam data using their MOIRCS data (Wang et al. 2009). On the other hand, Bundy et al. (2009) obtained relatively shallow K_s-band data with Subaru/MOIRCS and carried out the photometric calibration of their MOIRCS data using the Palomar/WIRC data (Bundy et al. 2005). Both studies used the MAG_AUTO from SExtractor as the total magnitude. In the figure, the K_s-band total magnitudes in the MODS catalog are slightly fainter on average than Barger et al. (2008) (by 0.04 mag) and Bundy et al. (2009) (by 0.10 mag), while the overall agreements are relatively good in the both cases. Considering the zero-point uncertainty, the total magnitudes are consistent among the studies.

Figure 18 shows comparisons of $U-K_s$, $B-K_s$, $V-K_s$, $i-K_s$, and $z-K_s$ colors between Barger et al. (2008) and this study. It should be noted that Barger et al. (2008) used MAG_AUTO for the color measurements, while the aperture diameter of 1.2 arcsec is used for the MODS data (the wide catalog). Despite the difference of the aperture size, these colors agree well, especially in the colors between the MOIRCS K_s band and the HST/ACS $BViz$ bands. For U-band photometry, we used the aperture correction with the surface brightness profiles of the B-band image, and the photometric error tends to be relatively large. The average difference of 0.12 mag in the $U - K_s$ color between Barger et al. (2008) and this study is expected from the uncertainty, and it may be due to some small systematic effect in the aperture correction. On the other hand, Figure 19 compares the $B - K_s$, $V - K_s$, $i - K_s$, and $z - K_s$ colors between Bundy et al. 2009 and our catalog. We again used the aperture magnitude with a 1.2 arcsec diameter for the MODS data and adopted the aperture magnitude with a 2.0 arcsec diameter from the catalog of Bundy et al. (2009). An excellent agreement can be seen in all the colors.

Figure 20 compares $K_s - [3.6]$, $K_s - [4.5]$, $K_s - [5.8]$, and $K_s - [8.0]$ between Wang et al. (2010) and this study. Wang et al. (2010) used a deconvolution procedure with a model image made from the convolved K_s-band image, which is similar with that used in the subtraction of the contribution from neighboring sources in our photometry (Section 5.2). On the other hand, we simply performed the aperture photometry after subtracting the contribution from neighboring sources and then applied the aperture correction with the surface brightness profiles of the K_s-band images. These colors agree relatively well within the uncertainty, although the colors in the MODS catalog tend to be bluer than those by Wang et al. (2009) at relatively red colors, and redder at the bluest colors, especially in the $K_s - [3.6]$ and $K_s - [4.5]$ colors. These systematic differences may be due to the differences in the method of the color measurement.
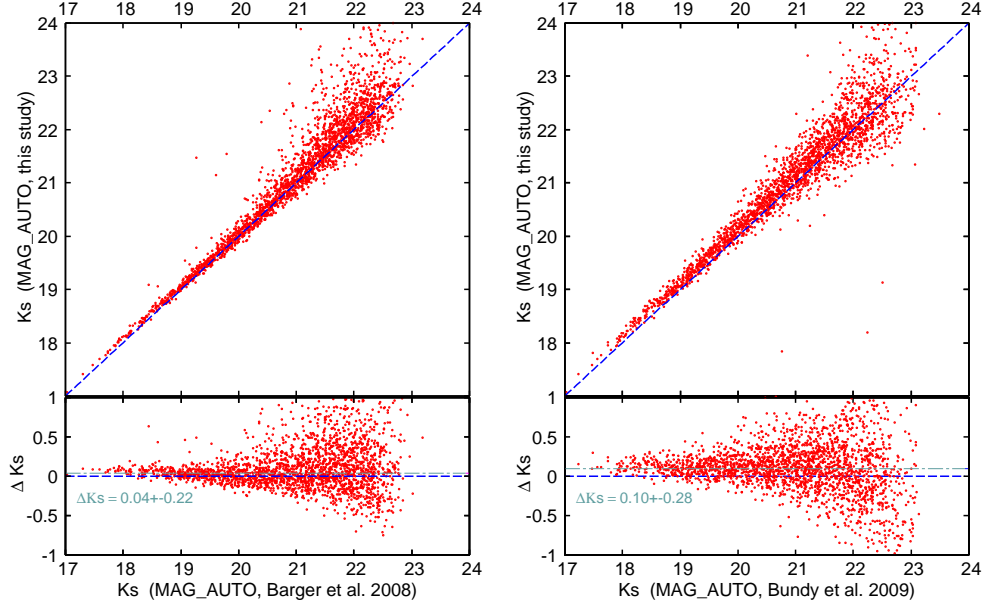
Fig. 17. Comparisons of the total K_s-band magnitudes (MAG_AUTO) in this study with those by Barger et al. (2008) (left) and by Bundy et al. (2009) (right).
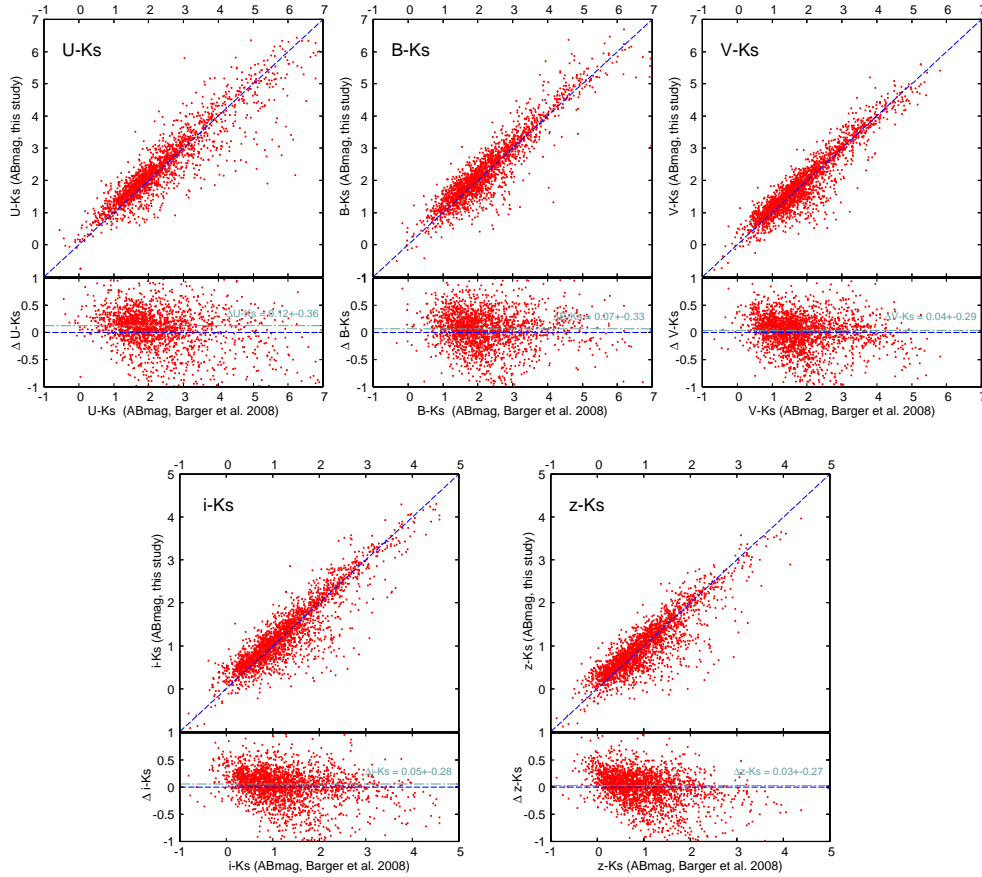

Fig. 18. Comparisons of $U - K_s$, $B - K_s$, $V - K_s$, $i - K_s$, and $z - K_s$ colors between this study and Barger et al. (2008). It should be noted that the colors from Barger et al. (2008) are measured with the Kron aperture (MAG_AUTO), while those for the MODS are measured with a 1.2 arcsec diameter aperture.
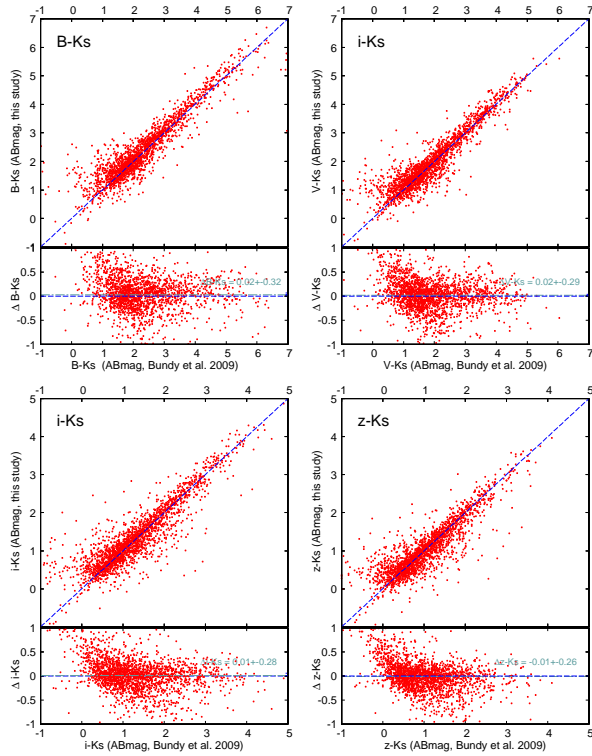
Fig. 19. Comparisons of $B - K_s$, $V - K_s$, $i - K_s$, and $z - K_s$ colors between this study and Bundy et al. (2009). While the colors in this study are measured with a 1.2 arcsec diameter aperture, those from Bundy et al. (2009) are measured with a 2.0 arcsec diameter aperture.
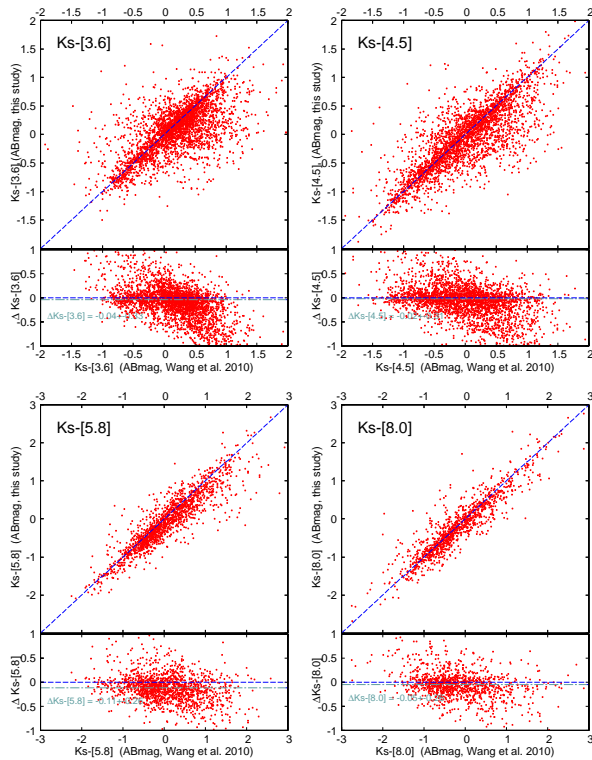

Fig. 20. Comparisons of $K_s - [3.6]$, $K_s - [4.5]$, $K_s - [5.8]$, and $K_s - [8.0]$ colors between Wang et al. (2010) and this study.

References

Alexander, D. M., et al. 2003, AJ, 126, 539

Barger, A. J., Cowie, L. L., & Wang, W.-H. 2008, ApJ, 689, 687

Bertin E., Arnouts S., 1996, A&AS, 117, 393

Brammer, G. B., van Dokkum, P. G., & Coppi, P. 2008, ApJ, 686, 1503

Bruzual G., Charlot S., 2003, MNRAS, 344, 1000

Bundy, K., Ellis, R. S., & Conselice, C. J. 2005, ApJ, 625, 621

Bundy, K., Fukugita, M., Ellis, R. S., Targett, T. A., Belli, S., & Kodama, T. 2009, ApJ, 697, 1369

Calzetti, D., Armus, L., Bohlin, R. C., Kinney, A. L., Koornneef, J.,

Capak, P., et al. 2004, AJ, 127, 180

Cohen, J. G. 2001, AJ, 121, 2895

Cohen, J. G., Hogg, D. W., Blandford, R., Cowie, L. L., Hu, E., Songaila, A., Shopbell, P., & Richberg, K. 2000, ApJ, 538, 29

Conselice, C. J., et al. 2007, ApJL, 660, L55

Cowie, L. L., Barger, A. J., Hu, E. M., Capak, P., & Songaila, A. 2004, AJ, 127, 3137

Cristóbal-Hornillos, D., Balcells, M., Prieto, M., Guzmán, R., Gallego, J., Cardiel, N., Serrano, Á., & Pelló, R. 2003, ApJ, 595, 71

Cristóbal-Hornillos, D., et al. 2009, ApJ, 696, 1554

Davis, M., et al. 2007, ApJL, 660, L1

Dawson, S., Stern, D., Bunker, A. J., Spinrad, H., & Dey, A. 2001, AJ, 122, 598

Dickinson, M., Papovich, C., Ferguson, H. C., & Budavári, T. 2003, ApJ, 587, 25

Fioc, M., & Rocca-Volmerange, B. 1997, A&A, 326, 950

Förster Schreiber N. M., et al., 2006, AJ, 131, 1891

Franx M., et al., 2003, ApJ, 587, L79

Giavalisco M., et al., 2004, ApJ, 600, L93

Grazian, A., et al. 2006, A&A, 449, 951

Greve, T. R., Pope, A., Scott, D., Ivison, R. J., Borys, C., Conselice, C. J., & Bertoldi, F. 2008, MNRAS, 389, 1489

Ichikawa T., et al., 2006, in Proc. of SPIE, Vol. 6269, 38

Ichikawa, T., et al. 2007, PASJ, 59, 1081

Ichikawa, T., et al. 2010, ApJ, 709, 741

Kajisawa, M., et al. 2006a, PASJ, 58, 951

Kajisawa, M., Kodama, T., Tanaka, I., Yamada, T., & Bower, R. 2006b, MNRAS, 371, 577

Kajisawa, M., et al., 2009, ApJ, 702, 1393

Kajisawa, M., Ichikawa, T., Yamada, T., Uchimoto, Y. K., Yoshikawa, T., Akiyama, M., & Onodera, M. 2010, ApJ, 723, 129

Kajisawa, M., et al., 2011, PASJ, submitted

Konishi, M., et al. 2010, arXiv:1009.3377

Labbé I., et al., 2003, AJ, 125, 1107

Le Floc'h, E., et al. 2005, ApJ, 632, 169

Leggett, S. K., et al. 2006, MNRAS, 373, 781

Madau, P. 1995, ApJ, 441, 18

Maihara, T., et al. 2001, PASJ, 53, 25

Maraston, C. 2005, MNRAS, 362, 799

Minowa, Y., et al. 2005, ApJ, 629, 29

Morrison, G. E., Owen, F. N., Dickinson, M., Ivison, R. J., & Ibar, E. 2010, ApJS, 188, 178

Perera, T. A., et al. 2008, MNRAS, 391, 1227

Pope, A., et al. 2006, MNRAS, 370, 1185

Quadri, R., et al. 2007, AJ, 134, 1103

Quadri, R. F., Williams, R. J., Lee, K.-S., Franx, M., van Dokkum, P., & Brammer, G. B. 2008, ApJL, 685, L1

Reddy, N. A., Steidel, C. C., Erb, D. K., Shapley, A. E., & Pettini, M. 2006a, ApJ, 653, 1004

Retzlaff, J., Rosati, P., Dickinson, M., Vandame, B., Rité, C., Nonino, M., Cesarsky, C., & GOODS Team 2010, A&A, 511, A50

Salpeter, E. E. 1955, ApJ, 121, 161

Scoville, N., et al. 2007, ApJS, 172, 1

Stetson, P. B. 1987, PASP, 99, 191

Suzuki, R., et al. 2008, PASJ, 60, 1347

Tanaka, I., et al., 2011, PASJ, submitted

Thompson, R. I., Storrie-Lombardi, L. J., Weymann, R. J., Rieke, M. J., Schneider, G., Stobie, E., & Lytle, D. 1999, AJ, 117, 17

Thompson, R. I., et al. 2005, AJ, 130, 1

Treu, T., Ellis, R. S., Liao, T. X., & van Dokkum, P. G. 2005, ApJL, 622, L5

Wang, W.-H., Barger, A. J., & Cowie, L. L. 2009, ApJ, 690, 319

Wang, W.-H., Cowie, L. L., Barger, A. J., Keenan, R. C., & Ting, H.-C. 2010, ApJS, 187, 251

Williams R. E., et al., 1996, AJ, 112, 1335

Williams, R. E., et al. 2000, AJ, 120, 2735

Williams, R. J., Quadri, R. F., Franx, M., van Dokkum, P., & Labbé, I. 2009, ApJ, 691, 1879

Windhorst, R. A., et al. 2010, arXiv:1005.2776

Wirth, G. D., et al. 2004, AJ, 127, 3121

Yamada, T., et al. 2009, ApJ, 699, 1354

Yoshikawa, T., et al. 2010, ApJ, 718, 112